Laser excited Li Rydberg atoms in electric and magnetic fields

Abdul Waheed

Dissertation for the degree of Philosophiae Doctor (PhD)

Department of Physics and Technology
University of Bergen, Norway

January 2012

Acknowledgements

All praises and thanks to almighty *ALLAH* for giving me the strength and spirit to complete my research in the field of laser spectroscopy. The development and completion of this work would not have been possible without the support and encouragement of a number of individuals to whom I would like to thank. First of all, I would like to sincerely thank my supervisor, Associate Prof. Øyvind Frette for his valuable insights, enthusiasm, support and continuous encouragement during the development of this work. I greatly appreciate the time that he spent and his effort for guiding me through this research experience and providing me a excellent research environment during my PhD studies.

I would like to express my deep gratitude to prof. Erik Horsdal, I am thankful for his inspiration, continuous support, encouragement and excellent guidance during my PhD studies. I am also grateful for the help and support from Daniel Fregenal. He helped me a lot to understand the equipment.

I greatly appreciate prof. Ladislav Kocbach for his kind support during my master and PhD studies and my co-supervisor prof. Jan Petter Hansen who provided me a opportunity to pursue my PhD studies in Norway. I am very thankful to Morten Førre for his support especially valuable theoretical discussion and helping me while writing an article together. I am very thankful to Jana Preclíková for reading through of my thesis, writing article and providing me a good company in the laboratory. I would also like to thank all my colleagues in the group of optics and atomic physics especially Lu Zhao, Stian Astad Sørngård and Børge Hamre for their support during my PhD studies. I am thankful to my friends Asif Javaid Wahla and Tahir Farooq for their cooperation and nice company.

It gives me great pleasure to express my gratitude to Higher Eduction Commission of Pakistan (H. E. C) for awarding me the Scholarship to complete PhD studies in the field of physics.

I am very grateful to my mother-in-law, brother Muhammad Riaz, Abdul Salam and uncle Abdul Razaq for providing me a moral support during last 4 years. I am deeply thankful to my parents who have always showered unconditional love on me, encouraged, and supported me in every aspect of life. It was my father's dream that I continue with PhD studies. He has always been my inspiration and I thank my mother, who, during difficult times stood by me and encouraged me to complete my PhD studies.

My special acknowledgement goes to my wife and children, Usama Waheed Tanoli and Saad Waheed Tanoli for being exceptionally patient and supportive during the difficult times of my PhD study and in particular my wife Shahnaz Waheed, who has given me a lovely daughter, Eshal Waheed Tanoli during the last year.

List of papers

1. I. Pilskog, D. Fregenal, Ø. Frette M. Førre, E. Horsdal and A. Waheed, *Symmetry and symmetry breaking in Rydberg-atom intrashell dynamics*, Phys. Rev. A. **83**, 043405 (2011)

2. A. Waheed, D. Fregenal, Ø. Frette, B. T. Hjertaker, E. Horsdal, M. Førre, I. Pilskog and J. Preclíková, *Suppression of multi-photon intrashell resonances in Li Rydberg atoms*, Phys. Rev. A. **83**, 063421 (2011)

3. J. Preclíková, A. Waheed, D. Fregenal, Ø. Frette, B. Hamre, B. T. Hjertaker, E. Horsdal, I. Pilskog and M. Førre, *Unidentified transitions in one-photon intrashell dynamics in Rydberg atoms*, submitted, Phys. Rev. A. (2012)

4. A. Waheed, I. Pilskog, D. Fregenal, Ø. Frette, M. Førre, B. Hamre, B. T. Hjertaker, E. Horsdal and J. Preclíková, *Intrashell RF-resonances in Li Rydberg atoms. Linear polarization and unexplained spectral features*, to be submitted, Phys. Rev. A (2012)

5. L. Kocbach and A. Waheed, *Visualization and studies of Rydberg states*, to be submitted, New Journal of Physics (2012)

Contents

Chapter 1

Introduction

The experimental work presented in this thesis has been carried out in the group of Optics and Atomic physics at the Department of Physics and Technology. The main purpose of the experiments have been to study the intrashell dynamic of the Li Rydberg atoms in the presence of perpendicular electric and magnetic fields.
Rydberg atoms are highly excited atoms with a single valence electron separated from the rest of the system (see figure 1.1). The valence electron, in high principal quantum number n, have binding energy that decrease as $\frac{1}{n^2}$, orbital radii that increase as n^2, and geometric cross-sections that scale as n^4 [1]. The excited valence electron is shielded from the electric field of the nucleus by the cloud of inner electrons.

When the valence electron is far from the ionic core (high angular momentum, l, states) it is only sensitive to the net charge, and behaves like the Hydrogen atom. On the other hand, when the valence electron comes near the ionic core (low-l, states) it can polarize and penetrate the ionic core. For this penetration of the inner core electrons, a correction term called the quantum defect is introduced. Since the Rydberg electron is very loosely bound to the core, minor perturbations will have significant influence on the electron's behaviour [2]. Even relatively weak external electromagnetic fields are strong enough to manipulate atomic states. Several papers have been published on this topic [3–9].

In [3] Mogensen et al., studied the lifetimes of Rydberg atoms formed by the adiabatic crossed-field method (ACFM). The dynamics of coherent elliptic states (*CES*) in time-dependent electric and magnetic fields has been studied by Kristensen et al [4]. The atomic pseudospins resonance in Li Rydberg atoms has been explained in terms of two independent pseudospins in two generalized magnetic fields in [6], whereas transient multiphoton resonances have been studied both experimentally and theoretically by Fregenal et al, and is presented in [7]. The dynamics of Stark-Zeeman split states in Li(n= 25) has been studied when the Rydberg atoms are exposed to a superposition of a slowly varying field and a harmonic RF-field in Pilskog et al [8]. While strong suppressions of the resonances are found (at certain values of the eccentricity e of the initial states) and shown in [9].

Rydberg atoms provide an experimental tool to explore the foundation of quantum mechanics. It is equally important to provide understanding of the gap between quantum physics and classical physics. It has already been demonstrated how to make classical states of atoms in the laboratory [10, 11]. These states have many of the properties of the classical picture of electron going around the core as proposed by

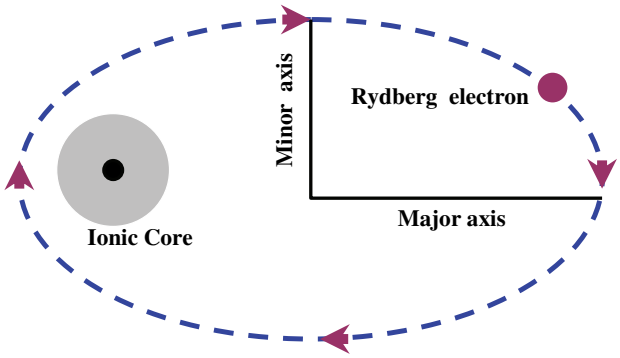

Figure 1.1: The classical representation of a Rydberg atom. The black dot symbolizes the nucleus, located in one of the focal points of the ellipse. The gray sphere is the cloud of inner-shell electrons and the red dot the electron exited to a Rydberg state.

Ernest Rutherford in 1911, and this was the starting point of Niels Boh'r model of the hydrogen atom [12]. An important step in the direction of classical limit was the work published by Schrödinger in 1926 [13] which states that in the limit of high quantum numbers it is possible to make an electron wavepacket with high degree of localization that travels on a classical path. He managed to make such states for the harmonic oscillator potential [14, 15]. Schrödinger then postulated that such states should exist for the Coulomb potential as well. So far all theoretical attempts have been unsuccessful in trying to construct these states, they may not even exist [16]. However, one has been able, both theoretically and also experimentally, to build so-called semi classical Rydberg states.

Semi classical states can be defined as states that have an electron density that follow a classical Kepler ellipse. The term coherent is used when quantum fluctuations are as small as possible considering the uncertainty relations. These coherent elliptic states (*CES*) are so far the closest analogous to a classical state of the hydrogen atom. They represent the point where classical and quantum mechanics meet. They are semi-classical because both classical and quantum mechanical arguments are used to construct them. One can construct these states experimentally by using the methods suggested by Delande and Gay [11].

In this thesis we introduce some of the well known basics of Rydberg atom physics which are indispensable for the understanding of Rydberg atom experiments. Extensive review of many aspects of the physics of highly excited atoms and molecules are given in [1] and [17].

Rydberg atoms can be prepared in coherent elliptic states (*CES*) of given eccentricity e and principal quantum number n by selective laser excitation followed by adiabatic transformation in weak electric and magnetic fields [3, 18]. The weak fields induce a definite Stark-Zeeman splitting of the n-shell and the *CES* considered here occupy the uppermost energy state of the Stark-Zeeman spectrum. Intra-shell transitions from initial *CES* to other states within the Stark-Zeeman spectrum can be induced by a variety of time-dependent fields. Multiphoton resonances were studied as a function of the eccentricity of the initial state in a recent experiment with Li-atoms excited to

n=25 and pulses of circularly polarized radio frequency (RF) fields [19].

Probabilities for electrons remaining in the initial state is studied as a function of the splitting of the shell at a constant RF-frequency. In such spectra multiphoton transitions show up as resonances. These were measured for a range of eccentricities with special emphasis on values close to one. Based on calculations using classical as well as quantum mechanics it is concluded that scattering off the non-hydrogenic core of the Li atom makes the electron dynamics chaotic. Chaos unfolds when the RF-field is sufficiently strong and long lasting, or when the eccentricity is large [20]. The plane of the circular polarization was defined by the major axis of the elliptic state and the normal vector of the elliptic orbit. In a purely hydrogenic picture this configuration leads to transition probabilities which are independent of eccentricity e. The variations actually observed for varying e are thus effects of the non-hydrogenic core. Linear polarization could not easily be accommodated in the experimental arrangement used previously [21]. To accommodate linear polarization a new arrangement with various electrodes has been built, and used in the experiments.

The objective of the present experimental work has been to study hydrogenic multiphoton transitions in a field configuration for which the transition probabilities depend on eccentricity e and the field strength of the linearly polarized RF-field. Constant orthogonal electric and magnetic fields were used to lift the degeneracy of the n-shell, and to define the eccentricity and orientation of the elliptic initial states. Transitions were driven by a linearly polarized RF-field of polarization parallel to the major axis of the elliptic state. The experimental results also show that the resonances generally are strongest for larger e values and very strong RF-field resulting in broadening and saturation.

The *CES* used in this experiment were prepared by exciting the uppermost state of the Stark-Zeeman spectrum. By laser tuning it is possible also to excite the neighboring energy state. This state is not a coherent state but the wave function still has elliptic shape, and can be characterized by an eccentricity. The probability distribution for an electron in a non-coherent state is less confined than in a coherent state and influenced more by the core. To investigate to what extent the results are sensitive to the core experiments with initial quasi-coherent elliptic states *qCES* has been performed.

In addition to the experimental work we also investigated the problems encountered when visualizing Rydberg states. In this work we focus on the Stark states, coherent elliptic states and quasi-coherent elliptic states of Rydberg atoms. We show some geometric interpretations of elliptic states which may be helpful in analysis of Rydberg state manipulations in external fields. Our demonstrations involve only hydrogen-like states. However, the techniques and analysis are also relevant for Rydberg molecules and more complicated highly excited atomic and molecular systems.

This thesis is structured in seven parts. Theoretical background about the Rydberg atom in external fields is discussed in chapter 2. In chapter 3, we present an overview of the experimental procedures and experimental setup for the production, manipulation, ionization and detection of Rydberg atoms. The special features of data acquiring, pulse timings and data analysis are presented in chapter 4. Chapter 5 introduces the scientific papers, which constitute the main part of the thesis and are found in chapter 7. Finally a conclusion and outlook on future perspectives of the experiment are given in chapter 6. Atomic unites are used (see appendix C).

Chapter 2

Theoretical background

2.1 Rydberg atoms in external electromagnetic fields

In this work we study lithium Rydberg atoms in weak time-dependent external electromagnetic fields. In the presence of the electromagnetic fields, and with the three tunable lasers we excite the Li atoms to the Rydberg state of n=25-shell or more specific, to the coherent elliptic state (*CES*) [18, 22, 23, 26], and its neighbouring states the quasi coherent elliptic states (*qCES*). The main qualitative difference between the two states is that a *CES* has maximum probability density along an elliptic path whereas a *qCES* has a node along the same path, and for a given eccentricity a *CES* has slightly smaller overlap with the core than a *qCES*. One of the defining properties of Rydberg atoms is their classical behaviour. The *CES* and the *qCESs* are some of the most classical states that are obtainable as their fluctuations are as small as possible considering the uncertainty relations [11, 25]. The *CES* and *qCES* were obtained by exciting an electron to the desired principal quantum number n=25 by tuning the infrared laser to a wavelength near 831 nm. The atoms were initially prepared to have an electron in a *CES* of given eccentricity determined by constant electric and magnetic fields orthogonal to each other, and the linear polarization was in the direction of the major axis of the *CES*. Atoms with an electron in a *qCES* or with equal mixtures of *CES* and *qCES* were also formed. The constant fields partially lifted the degeneracy of the n-shell and gave rise to a Stark-Zeeman energy splitting of the shell. The eccentricity, e of the initial *CES* or *qCES* can be determined by the expression;

$$e = \frac{3nE}{\sqrt{9n^2E^2 + B^2}}\,, \tag{2.1}$$

where E and B are the electric and magnetic fields, and n is the principal quantum number of the shell [18]. Eccentricity e of the initial state can thus be controlled by adjusting E & B-fields. If the B-field dominates in the system, the *CES* will have an eccentricity, $e \approx 0$, while when the electric field is dominating, $e \approx 1$. Eccentricity other than 0 & 1 can be obtained when the electric and magnetic fields have comparable values. Subsequently the cloud of the lithium Rydberg atoms in states of eccentricity given by 2.1 is exposed to the linearly polarised time-dependent electric field of radio-frequency (RF) [9]. When the frequency of the RF-filed resonates with the Stark-Zeeman splitting of the shell multiphoton transitions from the initial state *CES* or *qCES* to the other states within the shell are expected. At the end of the experiment, the

amount of Rydberg atoms that remains in the initial state are detected by the use of selective field ionisation (SFI) technique [1].

In the current chapter we first present some of the hydrogenic theory used in the following section. It is based on the reduction of the hydrogen Rydberg atom in weak external fields to a simple two-level system by exploiting the symmetries of the atom. In the section 2.3 we present the theory used for the external fields to drive the Rydberg electron into the core-region and the lithium nucleus must be taken into account. This causes the symmetries to be broken, and the non-hydrogenic core needs to be considered.

2.2 The hydrogen atom in external fields

In this thesis we investigated the lithium Rydberg atoms, when one of the single valence electron in a high principal quantum number, n=25, state. An electron in such a state is shielded from the electric field of the nucleus by the electrons in the ion core of a Rydberg atom. Therefore the excited electron sees the nucleus with only one proton, like the electron of a Hydrogen atom. Therefore such atoms share many properties with its hydrogen counterpart, and the extensive theories developed for hydrogen atoms in external fields can be used to solve the highly excited lithium atoms as well. In the semi-classical approximation, the Hamiltonian for atomic hydrogen interacting with the classical electric (E) and magnetic (B) fields is given by

$$H = H_0 + \mathbf{E}\cdot\mathbf{r} + \frac{1}{2}\mathbf{B}\cdot\mathbf{L}, \tag{2.2}$$

with

$$H_0 = -\frac{\nabla^2}{2} - \frac{1}{r}, \tag{2.3}$$

being the Hamiltonian of an unperturbed hydrogenic atom, and the angular momentum operators of the electron is given by $\mathbf{L} = \mathbf{r}\times\mathbf{p}$. In this thesis we worked with the intrashell dynamics only, and calculations can be restricted to be within the given n-manifold. When the electric and magnetic fields are sufficiently weak and the time variation of the fields slow, an electron initially excited into an arbitrary Rydberg n-shell cannot escape, from the given manifold, i.e. no intershell dynamics is allowed. The criteria to keep the dynamics intrashell can be formulated as follows: The maximal Stark and Zeeman energy splittings must be much smaller than the field-free energy separation between the manifold and the closest neighboring n-shells, i.e.,

$$3n^2E \ll \frac{1}{n^3},$$
$$\textit{and}$$
$$nB \ll \frac{1}{n^3}.$$

Furthermore, the frequency, ω, of the fields must be much smaller than the typical frequency between the neighbouring shells,

$$\omega \ll \frac{1}{n^3}.$$

Moreover the theory utilized in this section depend on the dynamics restricted to the given n-manifold. This includes the hydrogenic weak field theory presented in 2.2.1.

2.2.1 Hydrogen Rydberg atoms in weak slowly varying electromagnetic fields

In the week fields, the symmetry of the Coulomb potential can be utilized. In 1926 Wolfgang Pauli presented the problem of a hydrogen atom in external fields [27]. Here he showed that in the matrix formulation of quantum mechanics the stationary states of the hydrogen atom can be expressed as matrices. The Laplace-Runge-Lenz vector is a conserved physical quantity that controls the motion of any object which is under the influence of a central potential, like that of the hydrogen atom, and it points in the direction of the perihelion [24]. The wave mechanics was investigated by using the angular momentum operator, $\mathbf{L}$, and the Runge-Lenz vector, $\mathbf{A}$ by Demkov et al. The Work done by Demkov et al. [29] was carried further by Kazansky and Ostrovsky, and they showed that the intrashell dynamics within a single hydrogenic shell can be reduced to that of two independent spin-1/2 systems [31]. Finally, Førre et al, gave an explicit formula for transformation of amplitude from spin space to r-space [34]. In the previous section the Hamiltonian is given by the semi-classical expression, equation 2.2. As the dynamics is restricted to a single hydrogenic n-shell the Pauli's operator replacement can be applied [27–30],

$$\mathbf{r} = \frac{3}{2} n \mathbf{A}, \tag{2.4}$$

where $\mathbf{A}$ is the quantum mechanical counterpart of the classical Runge-Lenz vector,

$$\mathbf{A} = \frac{1}{\sqrt{-2H_0}} \left[\frac{1}{2} (\mathbf{p} \times \mathbf{L} - \mathbf{L} \times \mathbf{p}) - \frac{\mathbf{r}}{r} \right]. \tag{2.5}$$

We now, define two general spins (pseudospins),

$$\mathbf{J}_{\pm} = \frac{1}{2} (\mathbf{L} \pm \mathbf{A}) \ , \tag{2.6}$$

and performing the energy replacement, $H_0 = -1/2n^2$, the Hamiltonian for the intrashell dynamics can be reformulated into the form

$$H = \omega_+ \cdot \mathbf{J}_+ + \omega_- \cdot \mathbf{J}_- - \frac{1}{2n^2}, \tag{2.7}$$

$$H = \omega_+ \cdot \mathbf{J}_+ + \omega_- \cdot \mathbf{J}_-, \tag{2.8}$$

and the two effective magnetic fields are given by the following expression,

$$\omega_{\pm} = \omega_L \pm \omega_S = \frac{1}{2} \mathbf{B} \pm \frac{3}{2} n \mathbf{E} \ . \tag{2.9}$$

Where ω_L and ω_S are the Stark and Larmor frequencies, respectively, and can be defined by

$$\omega_S = \frac{3}{2} n E_{DC} \quad \text{and} \quad \omega_L = \frac{B}{2} \ . \tag{2.10}$$

The constant energy term $-1/2n^2$ in equation 2.7 is omitted in the following by a redefinition of the zero energy level. The operators $\mathbf{J}_\pm$ obey ordinary commutation relations for angular momentum operators [27, 29, 30]. They play the role of two independent spins, $\mathbf{J}_\pm^2|j_\pm m_\pm\rangle = j(j+1)|j_\pm m_\pm\rangle$ with $j=(n-1)/2$, rotating in the effective "magnetic fields" $\omega_\pm$, respectively. The eigenenergies of the Hamiltonian read [31]

$$E_{m_+,m_-} = m_+|\omega_+| + m_-|\omega_-|, \tag{2.11}$$

with $m_\pm = -(n-1)/2,\ -(n-1)/2+1, ..., (n-1)/2-1,\ (n-1)/2$. The eigenstates are uniquely defined by the quantum numbers n, m_+ and m_-. In the strong magnetic field limit (Zeeman limit) the quantum numbers are related to the magnetic quantum number m by $m = m_+ + m_-$, and in the strong electric field limit (Stark limit) to the Stark quantum number k by $k = m_+ - m_-$.

The solution of the Schrödinger equation with the Hamiltonian given by equation 2.8, could be obtained from two independent spin-1/2 systems [31]. The idea is based on the Majorana reduction of a general spin system [32, 33]. Majorana showed that there is a one-to-one correspondence between the solution of the spin j system in the field and $2j$ identical spin-1/2 systems rotating in the very same field. Formally the spin operators $\mathbf{J}_\pm$ become sums of spin-1/2 operators $S_\pm$,

$$\mathbf{J}_\pm = \sum_1^{2j} S_\pm \ . \tag{2.12}$$

From this, Kazansky and Ostrovsky showed that the solution to the full problem is dictated by the two-level Hamiltonians

$$H_\pm = \frac{1}{2}\begin{pmatrix} \omega_\pm^{(z)} & \omega_\pm^{(x)} - i\omega_\pm^{(y)} \\ \omega_\pm^{(x)} + i\omega_\pm^{(y)} & -\omega_\pm^{(z)} \end{pmatrix}, \tag{2.13}$$

where $\omega_\pm = [\omega_\pm^{(x)}, \omega_\pm^{(y)}, \omega_\pm^{(z)}]$, are the Cartesian components of the effective magnetic fields, $\omega_\pm$. The $\pm$ sign always refers to the $m_\pm$ quantum numbers, and that the total solution within the n manifold includes the solutions of two independent spin-1/2 systems.

2.2.2 Rydberg atoms in perpendicular electric and magnetic fields

In this thesis we worked with the electric and magnetic fields perpendicular to each other. In the present case with electric and magnetic fields in the xz-palne ($\mathbf{E} = E(t)\mathbf{e_x}$, $\mathbf{B} = B\mathbf{e_z}$), the two systems described by equation 2.13 are identical. The Hamiltonian for two-level system can then be written as

$$H_\perp = \frac{1}{2}\begin{pmatrix} \omega_L & \omega_S \\ \omega_S & -\omega_L \end{pmatrix} + \frac{1}{2}\omega_{RF}\, g(t)\cos(\Omega t)\begin{pmatrix} 0 & 1 \\ 1 & 0 \end{pmatrix}, \tag{2.14}$$

where ω_L and ω_S are defined in equation 2.10, and represent the constant electric and magnetic fields, when they are perpendicular the eccentricity, e, of the *CES* or *qCES* is define by

$$e = \frac{\omega_S}{\omega_{SZ}} \quad \text{and} \quad \omega_{SZ} = \sqrt{\omega_S^2 + \omega_L^2}\ , \tag{2.15}$$

The second term in equation 2.14 represents the linearly polarized RF-field which is responsible for driving intrashell transition from initial *CES* to the other states within the shell. Where g(t) is an envelope function of Gaussian shape with $\Omega = 2\pi f$ the angular frequency of the RF-field, and the strength is given by $\omega_{RF} = (3/2)n\mathbf{E}_{RF}$.

In present work, a coherent elliptic state (*CES*) is assumed to be populated at some initial time t_0. This corresponds to states defined by the quantum numbers $|m_+| = |m_-| = (n-1)/2$. Then, the (adiabatic) probability to remain in the initial state at some time $t > t_0$, after interaction with the external fields, is simply given by [31, 34]

$$P_a(t) = (1-p_+)^{n-1}(1-p_-)^{n-1}, \tag{2.16}$$

where $p_\pm(t)$ are the probabilities of transition in the corresponding spin 1/2 systems that is obtained by solving the time-dependent Schrödinger equation with the Hamiltonian given by equation 2.13.

2.3 Lithium Rydberg atoms in weak slowly varying electromagnetic fields

2.3.1 Quantum calculations for lithium

As it is mentioned in the previous section, the fields are weak enough to keep the Rydberg electron within the given *n*-shell and it is sufficient to apply the frozen-core approximation criteria. In this approximation the core electrons are considered not to be affected by the external fields. A lithium atom with one electron in a highly excited Rydberg state is conveniently modelled as a hydrogen-like system where the hydrogenic energy levels are (slightly) modified due to the presence of the core [1],

$$H = H_0 + V_c(r). \tag{2.17}$$

Where H_0 is defined by the equation 2.3, and $V_c(r)$ is a short-range, spherically symmetric potential representing the effect of two core electrons.

$$E_n \rightarrow E_{n,l} = -\frac{1}{2(n-\delta_{nl})^2}. \tag{2.18}$$

Here δ_{nl} are the so called quantum defects that account for the shift of the energy levels. Note that the degeneracy of the *n*-shell is lifted by the inclusion of core effects, i.e., the energy levels become *l*-dependent. The quantum defects δ_{nl} have an important effect on low angular momentum states in particular, as these states penetrate into the core region. For highly excited states they become almost independent on *n*, and for lithium they are approximately given by

$$\begin{aligned} \delta_s &= 0.3995 \\ \delta_p &= 0.0472 \\ \delta_d &= 0.0021 \\ \delta_f &= 0.0003 \end{aligned}$$

The quantum defects corresponding to $l > 3$ are so small that they may be ignored [21].

2.3.2 Basis expansion and coupling elements

The time dependent Schrödinger equation is given by the expression,

$$i\frac{\partial}{\partial t}\Psi(\mathbf{r},t) = H\Psi(\mathbf{r},t), \tag{2.19}$$

where Ψ is the wavefunction and H is the Hamiltonian that models the full system used in this work. The full Hamiltonian for lithium Rydberg atoms in electromagnetic field, can be written as

$$H = -\frac{\nabla^2}{2} - \frac{1}{r} + V_c(r) + \mathbf{E}(t)\cdot\mathbf{r} + \frac{1}{2}\mathbf{B}\cdot\mathbf{L}. \tag{2.20}$$

The core breaks the dynamical symmetry of the shell, which is essential for the hydrogenic theory described in the previous section, with the consequence that the reduction into two spin 1/2 systems are no longer possible. Instead, such a problems can be solved by expanding the time-dependent wave function in a set of functions that are not themselves solutions to the problem in hand. This in braket notation is called as basis expansion method, and the total state vector, can be written in the form,

$$|\Psi(t)\rangle = \sum_{lm} c_{lm}(t)|nlm\rangle, \tag{2.21}$$

where the set of hydrogenic basis functions, $\{|nlm\rangle\}$, spans the full n-manifold. As mention before the fields are restricted to only drive intrashell dynamics, the basis can be limited to only describe the given n-shell.

The basis expansion is performed by inserting equation 2.21 into equation 2.20. The time dependent Schrödinger equation can then be written as a set of coupled differential equations,

$$i\hbar\frac{d}{dt}c_{lm} = \sum_{l'm'}\langle nlm|H|nl'm'\rangle c_{l'm'}, \tag{2.22}$$

The coupling elements of equation 2.20 are well known. In this work a Cartesian coordinate system is chosen such that the magnetic field points along the positive z axis and the electric field is parallel to the x axis. Moreover, the linearly polarized RF-pulse that drives the multiphoton transitions is parallel to the DC electric field. Finally, in order to account for a small stray field, the DC electric field is assumed to also have a small component parallel to the magnetic field. The Hamiltonian can therefore be expressed as,

$$H = H_0 + V_c + E_x x + E_z z + \frac{1}{2}B_z l_z. \tag{2.23}$$

As the fields are not space dependent and they have no affect on the matrix elements except as scaling factors. The matrix elements can therefore be written as,

$$\begin{aligned}\langle nlm|H|n'l'm'\rangle &= \langle nlm|H_0 + V_c + E_x x + E_z z + \frac{1}{2}B_z l_z|n'l'm'\rangle & (2.24)\\ &= \langle nlm|H_0|n'l'm'\rangle + \langle nlm|V_c|n'l'm'\rangle + E_x\langle nlm|x|n'l'm'\rangle \\ &+ E_z\langle nlm|z|n'l'm'\rangle + \frac{1}{2}B_z\langle nlm|l_z|n'l'm\rangle & (2.25)\end{aligned}$$

where n, l and m are the hydrogenic quantum numbers. The first term of the equation 2.25 is the hydrogenic energy which is defined by

$$\langle nlm|H_0|nlm\rangle = -\frac{1}{n^2}\delta_{ll'}\delta_{mm'} \,. \tag{2.26}$$

The second component of equation 2.25 is the correction term which modifies the relevant diagonal elements, equation 2.18. Then the (non-zero) dipole coupling elements are given by [35],

$$\begin{aligned}
\langle nlm|E_x x|nl-1m\pm 1\rangle &= \mp\frac{3}{2}nE_x\sqrt{\frac{(l\mp m-1)(l\mp m)(n^2-l^2)}{4(4l^2-1)}} \\
\langle nlm|E_z z|nl-1m\rangle &= -\frac{3}{2}nE_z\sqrt{\frac{(l^2-m^2)(n^2-l^2)}{4l^2-1}} \\
&\textit{and} \\
\langle nlm|B_z|nlm\rangle &= mB_z.
\end{aligned}$$

With these matrix elements in place it is straight forward to solve equation 2.22 numerically.

Chapter 3

Experimental setup and procedures

The experimental setup consists of two vacuum chambers with various experimental facilities and three dye lasers pumped by a pulsating pump laser. The light from the three dye-lasers selectively excite Li-atoms produced in the vacuum system to specific Rydberg states which are perturbed by an electric field. We first discuss the components of the vacuum systems and then the laser system. A new vacuum system was developed for the experiment.

3.1 The vacuum chambers and their components

The vacuum system is shown as a 3-D image in figure 3.1A and a schematic diagram of the various electrodes necessary for conducting the experiments may be found in figure 3.1B.

The vacuum system consist of two chambers separated by a valve and pumped by two turbomolecular pumps (TMU 261 and TURBOVAC 50) supported by two rotary pumps, one pair of turbomolecular and rotary pump for each chamber. The lower chamber holds an electrically heated oven which produces a thermal beam of Li-atoms, and in the upper chamber one finds a number of electrodes which support a range of electric fields used in the experiments to form and manipulate Rydberg atoms, and a detection arrangement for such atoms. All electrodes and other materials seen by the Rydberg atoms are cooled to the temperature of liquid nitrogen to suppress interaction with the blackbody radiation from these materials [27]. Outside the upper vacuum chamber there is a set of coils which produce a magnetic field when excited by a current. This field extends throughout the vacuum system. In the following subsections the different components of the vacuum system are discussed in more detail.

3.1.1 Turbomolecular pumps

Two turbomolecular pumps TMU 261 [38] and TURBOVAC 50 [39] are installed in the upper and lower chambers of the vacuum system. Turbo pumps generate vacuums in the high to ultra-high vacuum range of up to 10^{-11} mbar. To attain high vacuum (HV), we use two different pumps: a rotary pump and turbomolecular pump. The turbomolecular pump reduces the pressure from about 10^{-3} to 10^{-7} mbar.
The basic working principle of the turbomolecular pump is similar to that of a turbine with blades [36]. The rapidly rotating rotor transfer momentum to the gas molecules,

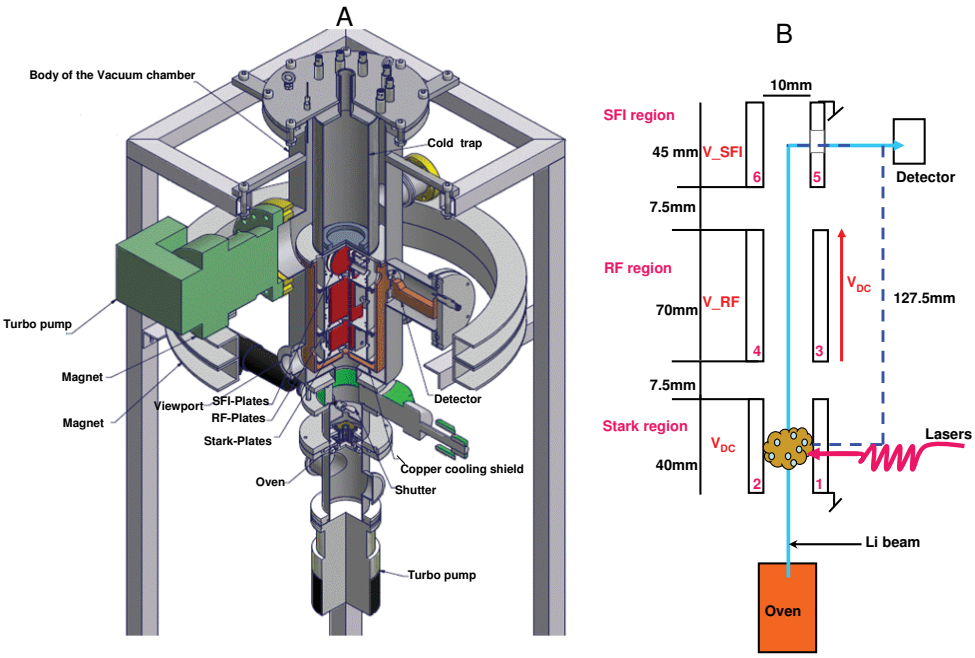

Figure 3.1: A 3-D view of the inside of a vacuum chamber shown in panel A, and the most essential parts are shown in the schematic diagram in panel B. In panel A, the upper chamber consist of the turbomolecular pump, a detector assembly and three pairs of parallel plates painted red. From the bottom to the top the first, second and third pair of plates form the Stark-region, RF-region and SFI-region respectively. The lower chamber contains the oven assembly and a turbomolecular pump, and separated from the upper chamber by green valve located above the oven assembly.

their initially non-directed thermal motion is changed to a directed motion. It consists of a stack of rotors with blades, or slots, depending on the specific pump. In between rotor disks are stators, fixed discs that contain the same blades, or slots, as the rotors, but oriented in the opposite direction. Lateral view of the inside of a turbo pump is shown in figure 3.2. The motor makes the rotor spin about the axis. The stators are fixed disks in between rotors, and the vent is a hole through which we can let a gas through if we wish to bring the pump back to a higher pressure. The big arrows show the flow of pumped molecules. To create the directed motion of the gas molecules, the tip of the roter blades have to move at a speed of 60000 rpm (about 2100 rad/s). When the blades, spinning at such a high speed, hit the molecules, they impart momentum on them. The rotor-stator pairs drive the molecules towards the exhaust, where they are collected by the rotary pump.
In our vacuum system the rotary pump and turbomolecular pump are electrically interconnected through the front panel of the vacuum controller which is shown in figure B.1 (see appendix B).

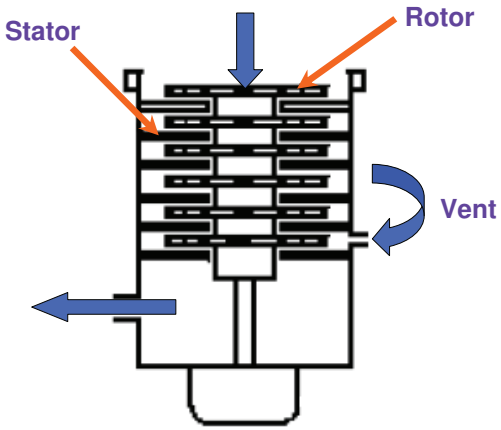

Figure 3.2: Lateral view of the inside of a turbo pump shown. The motor makes the rotor spin about the axis. The stators are fixed disks in between rotors, and the vent is a hole through which we can let a gas through if we wish to bring the pump back to a higher pressure. The big arrows show the flow of pumped molecules [37].

3.2 Li beam

A small piece (≈0.15 g) of metallic Li was loaded in the oven which was heated to ≈ 400°C with a pressure below $\leq 10^{-6}$ mb. The heated Lithium produces a vapour of atoms, which stream out of the oven and move into the vacuum chamber.

3.3 Excitation, manipulation and ionization of Rydberg atoms

We excite, manipulate, ionize and detect the Rydberg atoms in the upper chamber which consist of three different regions (see figure 3.3).

1. Stark-region
2. RF-region
3. SFI-region

3.3.1 Stark-region

In this region the Li beam is crossed at right angle by three tunable dye lasers in the presence of an electric field which is adjusted to produce the maximum possible Stark splitting of the n shell without inter mixing to the other n shells.

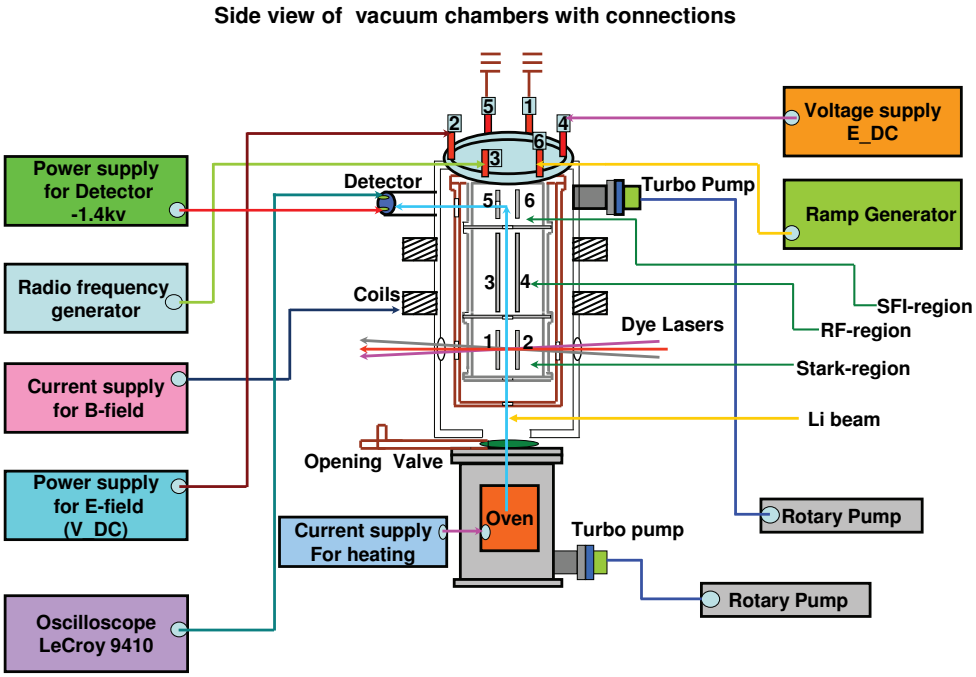

Figure 3.3: Side view of the vacuum chambers with necessary components. The lower chamber is separated from upper one by a green valve labelled as opening valve. Each chamber has a turbomolecular pump supported by a rotary pump. The lower chamber consists of an oven loaded with metallic Li which produces thermal Li beam when heated by an applied current. The upper chamber consists of three pairs of parallel plates (1-6) surrounded by a copper shield. Plates 1 & 2 form the Stark-region, 3 & 4 form the RF-region and 5 & 6 comprises the SFI region. Three tunable dye lasers cross the Li beam at right angle in the Stark-region and excite the Li atoms to the Rydberg states. Coils connected to the current supplies and the voltage supplies are the sources of B and E fields respectively. These fields are used to form, manipulate and detect the Rydberg atoms.

A DC-voltage V_{DC} was applied to plate no.2, and plate no.1 was grounded as shown in figure 3.3. This arrangement provide an electric field of $\approx$ 145 V/cm which is sufficient to produce maximum Stark splitting of n=25. In the presence of the electric field of $\approx$ 145 V/cm the three tunable lasers excite the Li atoms to the Rydberg state of n=25. The excitation scheme is shown in figure 3.4. The energy levels are denoted spectroscopically. The 2s is the ground state of Li. The arrows show dipole allowed resonant transitions. The notation $''25f''$ indicates excitation of the Stark state through it's f-character.

The infrared laser was tuned to a wavelength near 831 nm to excite the uppermost state of the Stark manifold or the state just below the uppermost state (see figure 3.4). The uppermost state is a Stark state of maximum polarization quantum number k, $|nkm\} = |25,24,0\}$ [1]. It has maximum electric dipole moment for the shell, and it is also a coherent elliptic state CES of eccentricity e=1. The degenerate states next to the uppermost state are $|nkm\} = |25,23,\pm 1\}$ [1]. They are quite similar to the uppermost

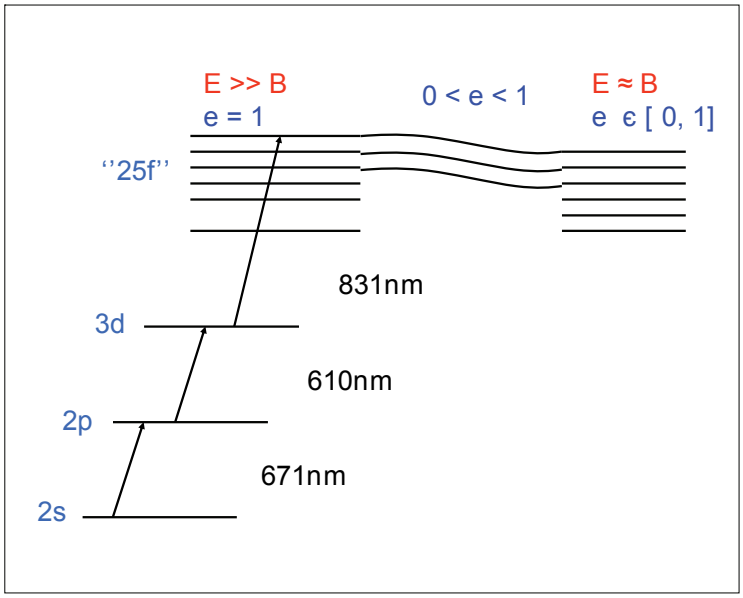

Figure 3.4: Excitation scheme and Rydberg Stark Zeeman states. To the left in the Stark-region the electric field dominates. To the right (in the RF-region) the electric and magnetic fields have comparable influence on the splitting of the shell.

state, and we refer to them as quasi-coherent elliptic states *qCES*.

The selective excitation of either of these states is possible only when the bandwidth of the infrared laser is smaller or comparable to the energy gap of 3.4 GHz at 145 V/cm between the relevant states. For this purpose we use a Fabry-Perot etalon which decreases the bandwidth of the 831 nm laser from 6.5 GHz to 3.3 GHz. After finishing the *CES* or *qCES* preparation the Stark-Zeeman states drift out of the Stark-region, and move into the RF-region with thermal mean velocity of $\approx$1.25 mm/μs . The horizontal distance between all the electrostatic plates are 10 mm, and the vertical distance from one set of plates to the next are 7.5 mm, and is shown schematically in figure 3.1B. The passage time for the cloud of Rydberg atoms from one region to another is of the order of 5 μs.

3.3.2 RF-region

While passing from the Stark region to the RF-region the cloud of Rydberg atoms experience gradual reduction of the electric field from 145 V/cm to approximately 1 V/cm in the presence of a perpendicular magnetic field of the order of 60 Gauss (=60·10^{-4} T), and transform adiabatically into coherent elliptic state (*CES*) of eccentricity e given by the equation

$$e = \frac{\omega_S}{\omega_{SZ}}, \tag{3.1}$$

where

$$\omega_{SZ} = \sqrt{\omega_S^2 + \omega_L^2}, \qquad \omega_S = \frac{3}{2} n E_{DC} \qquad \text{and} \qquad \omega_L = \frac{B}{2}. \tag{3.2}$$

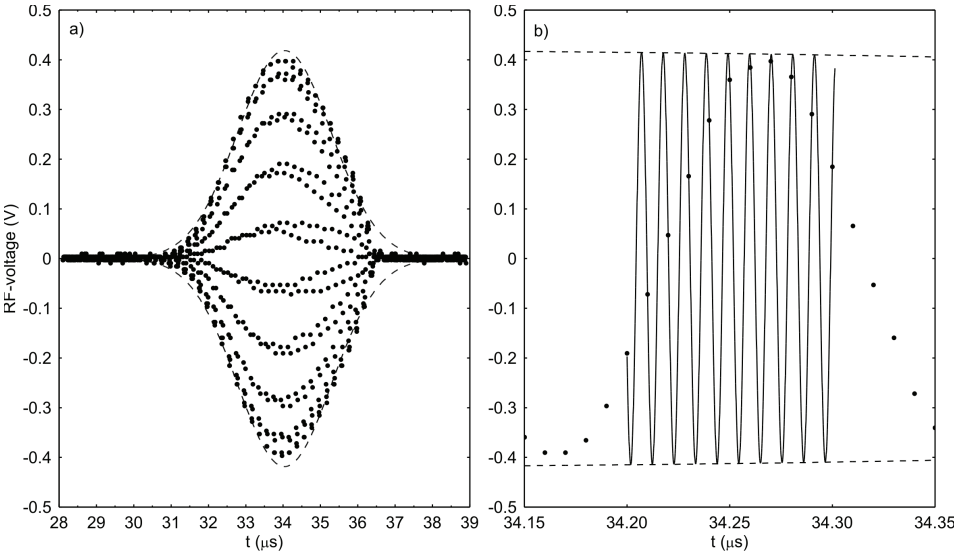

Figure 3.5: Pulse of harmonic voltage V_{RF}. a) Full pulse. b) Sample shown on expanded time scale near maximum. Full curve shows a fit to the measured points by a harmonic curve of the applied frequency. The dots are the values measured by the digital oscilloscope at the maximum sampling rate of 10 ns intervals.

Here ω_S and ω_L are the Stark and Larmor frequencies, respectively, and atomic units are used. At n=25, 1 V/cm corresponds to $\omega_S = 2\pi \cdot 48 \times 10^6$ rad/s, and 60×10^{-4} T to $\omega_L = 2\pi \cdot 84 \times 10^6$ rad/s. See also appendix C. The transformation is adiabatic if $\frac{\dot{\omega}_S}{\omega_S} \ll \omega_{SZ} = \frac{\omega_S}{e}$ or $\frac{\dot{\omega}_S}{\omega_S} \ll \omega_S$. At the present rate of decrease of the electric field $\frac{\dot{\omega}_S}{\omega_S} = 0.2$ Mc/s and a splitting corresponding to 1 V/cm or 35 Gauss, $\omega_S = 2\pi \cdot 84 \times 10^6$ 1/s= 300 Mc/s it is clear that the transformation must be adiabatic. When the cloud of Rydberg atoms in coherent elliptic states (*CES*) of eccentricity given by the equation 3.1 comes near to the center of the RF-region, 30 μs after the laser shot, the *CES* are exposed to the RF-field. The source of this field is a harmonic voltage V_{RF} applied to plate no. 3 (see figure 3.3) for a short period of time t≈5 μs, to produce a pulse of linearly polarized electric field E_{RF} as shown in figure 3.5 [9].

This linearly polarized electric field is responsible for driving intrashell transitions from an initial *CES* to the other states within the shell. When the frequency of the applied RF-field was on resonance with the Stark-Zeeman splitting of the shell ($2\pi N f = \omega_{SZ}$) where f is the frequency of the RF-field and N=1, 2, 3, 4 $\cdots$ multiphoton transitions from initial *CES* to the other states within the shell was seen as shown in figure 3.6.

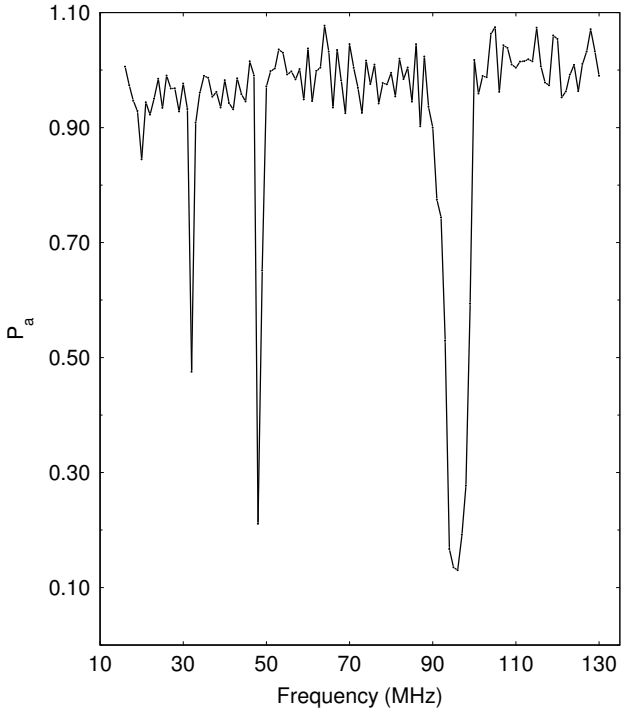

Figure 3.6: Adiabatic probability P_a vs frequency f of the harmonic field. N-photon resonances with N=1, 2, 3 and 4 are seen near f=95, 48, 33 and 26 MHz, respectively.

Here the adiabatic probability P_a vs frequency f of the linearly polarized harmonic field for n=25 with fields strength $\approx$ 0.440 V/cm is shown. P_a is the probability that the Rydberg atoms remain in the initial state after the RF-field. The probability P_a deviates from 1 typically when a multiple of the RF-frequency comes into resonance with the splitting of the shell. These resonances may saturate and get broadened with higher field strength and larger eccentricity. One must use a good RF-generator with no or only very weak higher harmonics because one photon transitions driven by the Nth harmonic can be misinterpreted as an N photon resonance.

3.3.3 SFI-region

After the cloud of Rydberg atoms move out of the RF region they enter into the SFI region. The effect of the B-field on the Rydberg atoms remains constant, but that of the E-field decreases as the Rydberg atom drift out of the RF-region and move into the SFI-region. The Rydberg atoms are detected in the SFI-region by selective field ionization [1]. The ionizing field is produced by a high-voltage pulse applied to plate no. 6 after t$\simeq$66 μs to the laser shots, and plate no. 5 is at ground potential (see figure 3.3). For this purpose, a linear ramp generator has been constructed based on a design of Fuqua and MacAdam [41]. Turn on of the ramp is slow, and almost follows a parabolic shape (see figure 3.7). This device generates a positive, linearly rising 3 kV

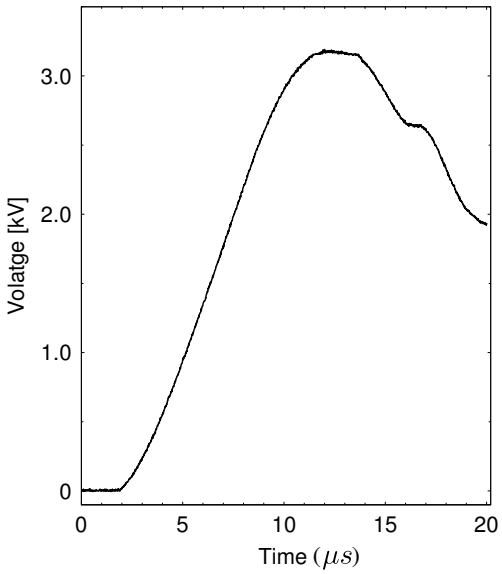

Figure 3.7: Output from the linear-ramp generator recorded with the digital oscilloscope. The time in (μs), and the ramp is triggered at t=60 μs after the laser shots.

pulse shown with a slew rate adjustable over the range from 100 to 500 V/μs. In this work, all data are recorded with a slew rate of 450 V/μs, and the ramp output for this setting is shown in figure 3.7.

The Li^+ ions produced by the field ionization will be accelerated through a hole in the grounded plate no. 5. and detected by a Channeltron detector. The hole is covered by a high transmission grid to keep the electric field between the plates homogeneous. After passing through the hole the ions are accelerated further onto the funnel of the Channeltron detector which is at -1.4 KV. The anode signal is taken out at ground potential and connected directly to one of the input channels of a LeCroy 9610 digital oscilloscope (see figure 3.3). The signal is averaged over typically 100 laser shots to form an SFI-spectrum.

3.4 Detection of Rydberg atoms by Selective field ionization

We collect SFI spectra at various experimental conditions. Detection of the Rydberg atoms by SFI is influenced by several experimental parameters which, in turn, may be very useful for identification. To take advantage of this, it is necessary to understand the evolution of the Rydberg state from dominant B-field coupling to a dominant E-field coupling for perpendicular fields.

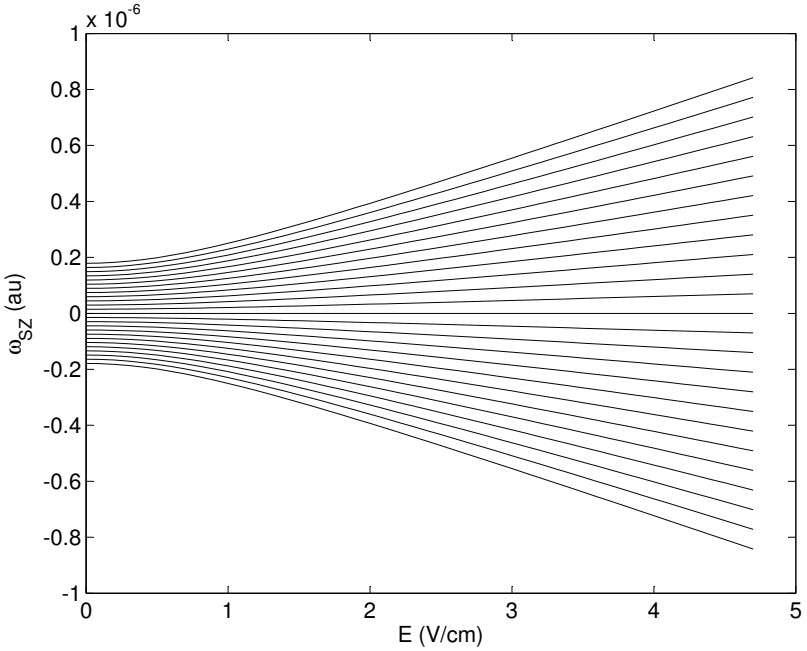

Figure 3.8: Schematic Stark-Zeeman spectrum as a function of external field. To the left the magnetic field dominates. While the levels show curvatures the electric and magnetic fields have comparable influence on the splitting of the shell [43]. To the right where the levels are straight lines the electric field dominates and eccentricity $e \approx 1$.

The ramp turns on sufficiently slowly that the adiabatic passage from dominant B to dominant E is adiabatic. Circular states thus turns into linear states. This is illustrated in figure 3.8 by the uppermost curve. When E (the ramp field) is increased further the region of intershell mixing is reached (see figure 3.11). In the case of Li, all Rydberg states with $|m|<2$ including *CES* and *qCES* will behave adiabatically in this region as shown in figure 3.11b, and states with $|m|>2$ behave diabatically [42] as shown in figure 3.11a.

Figure 3.9a shows an adiabatic SFI spectrum when the RF-field is on but off resonance with the Stark-Zeeman splitting ($2\pi f = \omega_{SZ}$) of the shell. When the resonance is off, the RF-field does not effect the *CES* or *qCES*, and there is no transition from initial state *CES* or *qCES* to the other states within the shell. The Spectrum shown in figure 3.9b is mostly diabatic. It is obtained when the RF-field is on resonance with the shell splitting. The population is distributed to the other states within the shell. Rydberg states with $|m|=2$ evolve adiabatically with a probability of about 50%. This makes it possible to distinguish states of $|m|<2$ from states of $|m|>2$. The former are unperturbed states and the latter those that have interacted with the RF-field. States that develop adiabatically eventually ionize at a relatively low field when the classical ionization limit is reached, while diabatic states ionize by tunnelling over a range of typically somewhat larger fields [1, 42, 45].

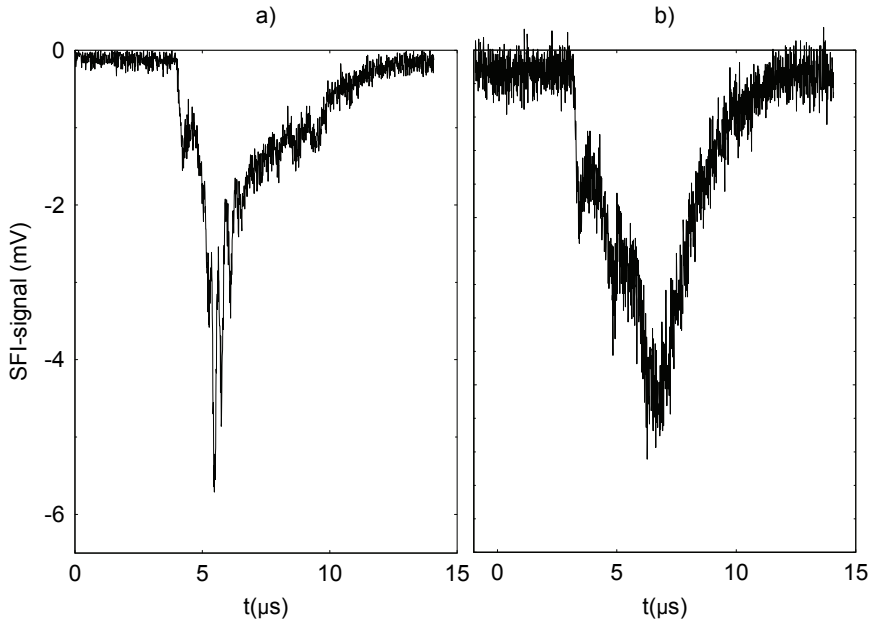

Figure 3.9: a) Adiabatic spectrum with RF-field off. b) Diabatic spectrum with RF-field on, shell splitting $2\pi f = \omega_{SZ}$=95MHz.

3.5 Classical (adiabatic) and non-classical (diabatic) field ionization

In this section we go into more detail with the SFI detection technique. The H atom with its nucleus at the origin in the presence of an electric field in the z-direction is shown in the figure 3.10. The potential (in atomic units) experienced by an electron moving along the z-axis is is given by [1].

$$V = -\frac{1}{r} + Ez, \tag{3.3}$$

where E is the magnitude of the applied field. Introduction of an electric field along the z-axis destroys the spherical symmetry of the potential shown by the red curve. It has a saddle point on the z-axis at z = -$\frac{1}{\sqrt{E}}$ where the potential has the value

$$V = -2\sqrt{E}. \tag{3.4}$$

For other than m=0 states there is an additional centrifugal potential ($\frac{1}{x^2+y^2}$), keeping the electron away from the z-axis. The centrifugal barrier raises the threshold field of $m \neq 0$ states [44]. For m=0 states with binding energy W, the ionization field is given by

$$E = \frac{W^2}{4}, \tag{3.5}$$

which is usually called the classical field-ionization limit [46]. Li atoms have similar characteristics to those of hydrogen atoms in the presence of electric field. But there are

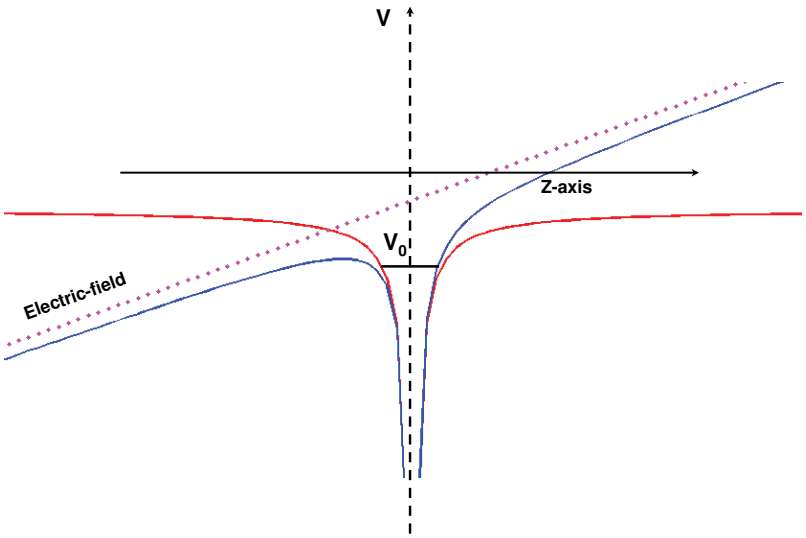

Figure 3.10: The Coulomb potential perturbed by an external electric field parallel to the z-axis.

important differences due to the presence of the finite sized ionic core. With no field the presence of the core simply depresses the energies, especially those of the lowest l. As long as the core is spherically symmetric, it does not alter the spherical symmetry of the problem, and the effect is relatively minor except for $l \leq 3$. However, with finite sized ionic core the wavefunction is no longer separable in parabolic coordinates. As a result the parabolic quantum number k, which is a good quantum number in H, is no longer good [1]. The Stark states with a positive Stark shift have the electron localized on the

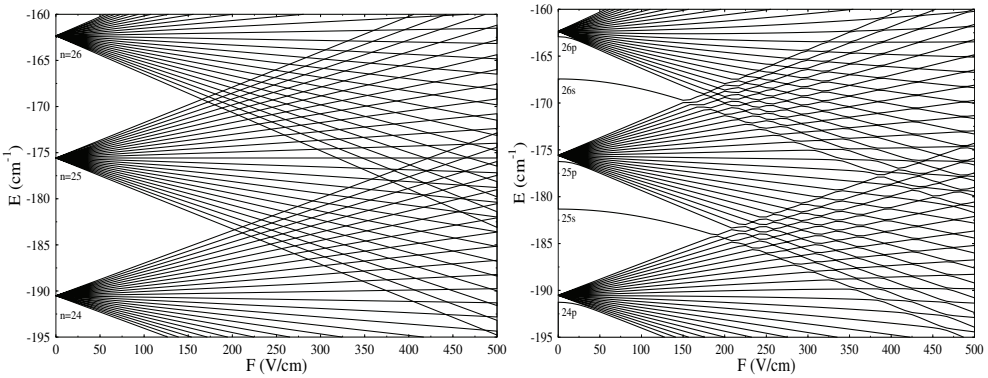

Figure 3.11: Energy levels for the Stark Hamiltonian of a) for hydrogen b) for lithium in the neighbourhood of n=25 for m=0 states [53].

side of the atom away from saddle point and are called blue states. The Stark states with a negative Stark shift have the electron localized adjacent to the saddle point and

are named red states. The most important implication of k not being a good quantum number is that blue and red states of $|m| \leq 2$ are coupled by their slight overlap at the core. In the inter shell mixing region below the classical ionization limit blue and red states of the adjacent n and $|m| \leq 2$ do not cross as they do in H, but exhibit avoided crossing as a result of their being coupled (see figure 3.11).

The red states field-ionize at the classical field-ionization level, whereas the blue states ionize by tunnelling over a range of typically somewhat larger fields. For more details see Bethe and Salpeter [35] or Gallagher [1]. When the ionization field (ramp field) increases to a certain point the eigenenergy curves from neighbouring shells approach each other (see figure 3.11a).

The presence of the core destroys the dynamical symmetry of H, and converts the level crossings to avoided crossings (see figure 3.11b) [34, 42]. This is, however, only the case for low l states which can be influenced by quantum defects. All states of $l \geq 3$ have negligible quantum defects which means that they are hydrogen-like and field-ionize diabatically (non classically). In the case of diabatic field-ionization the wavefunction is frozen. Whereas for the adiabatic field-ionization, the wavefunctions change their forms at the avoided crossings. It means that the cloud of electrons moves along the electric field towards the saddle point, and the atoms ionize at the classical ionization limit.

3.6 Photo electron multiplier Detector (Channeltron)

The Channeltron is a durable and efficient detector to detect ions or electrons. Figure 3.12 illustrates the basic structure and operation of the Channeltron. This structure is also known as (single) channel electron multiplier(CEM).

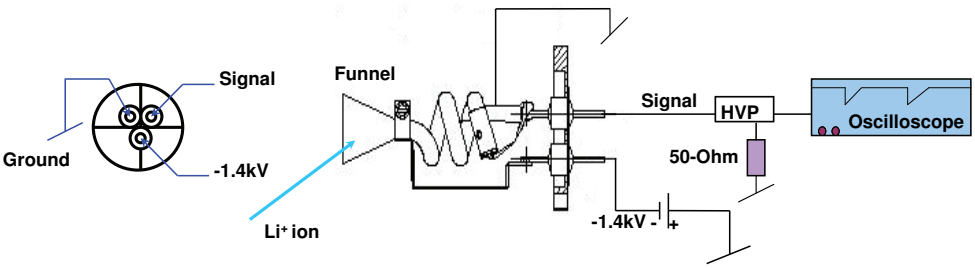

Figure 3.12: Schematic diagram of Channeltron for ion detection and secondary electrons production [47].

The operating principle of the Channeltron is illustrated in figure 3.12. It is built with a glass funnel coated inside with a thin film of semi-conducting material and a glass tube which is coated with a highly resistive material in the inside. A negative high voltage (-1.4 kV) is applied at the funnel and the collector is near ground (see figure 3.12). It used to establish a uniform electric field within the channel. When a Li^+ ion strikes the funnel secondary electrons are generated and accelerated by the electric field whereby their transverse velocity causes further impacts on the inner surface of

the tube, whilst the secondary electrons are carried along the tube by the longitudinal field. Since this transverse motion is combined with a longitudinal acceleration down the tube provided by the electric field, the result is a zigzag path in which the electrons successively strike opposite walls of the tube [48]. These secondary electrons each produce two electrons, two become four, and the numbers continue to increase until a pulse of 10^7 to 10^8 electrons emerges and are collected at the anode. The 50 Ω resistance converts current into a voltage which is measured by the oscilloscope. A high voltage protector (HVP) is used to protect the oscilloscope.

3.7 Lasers setup

Figure 3.13 shows a detailed drawing of the laser setup on the optical table.

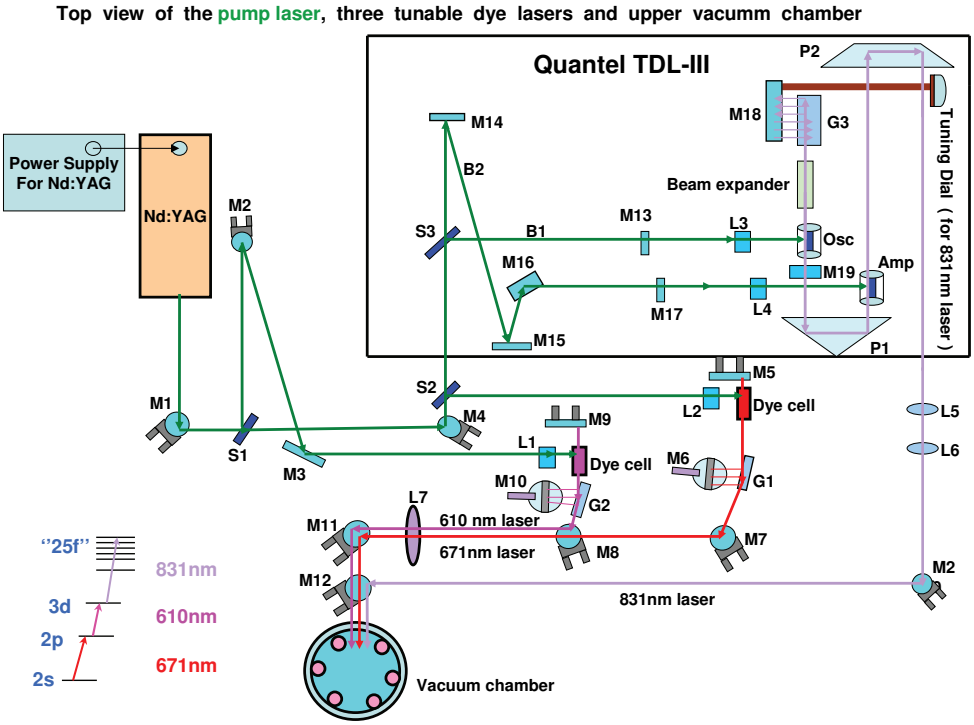

Figure 3.13: Schematic diagram of the laser setup on the optical table. There are four lasers shown in the diagram, the pumping source and the tunable dye lasers. The green one is the Nd:YAG laser used to pump three dye lasers shown pink, red and purple. Three collinear beams of dye lasers tuned near the wavelengths 671 nm, 610 nm, and 831 nm enter the vacuum chamber and cross the Li beam (not shown) at right angles and excite the Li atoms resonantly to a Rydberg state of n=25 according to scheme 2s→2p→3d→25f as shown in the figure.

Here we present an overview of the setup. They are four lasers shown in the figure 3.13. The light from the Nd:YAG laser is a pump source for three tunable dye

lasers. The first dye laser which is used to excite Li atoms from ground state to first excited state i.e. 2s to 2p state, is generated by the cavity which is made up of the mirror M5, the dye cell, the grating G1, and the tuning mirror M6. A grating at grazing incidence (that increases the spectral resolution of a dye laser) is used, and we tuned this laser light to a wavelength near 671 nm using M6. The output (laser light) from the laser cavity is the light that is reflected from the grating.
The light from the second dye laser is produced by the cavity comprising the mirror M9, the dye cell, grating G2 and the mirror M10, and the wavelength is tuned near 610 nm by using the mirror labelled M10. The tuned laser light from the laser cavity is fed into the vacuum where it resonantly excites the Li atom from 2p to 3d state.
The Quantel TDL-III pulse dye laser is the third dye laser in our laser system. It is used to excite the Li atoms from 3d to 25f state, which is the Rydberg state. The pumping beam is divided into two beams B1 and B2 at the splitter S3. The B1 is then focused into the dye circulating in the oscillator located in the laser cavity which is formed by the oscillator assembly consisting of beam expander, grating G3 and tuning mirror M18 and semi transparent mirror M19.

The laser light produced in the laser cavity is tuned by the rotating mirror (M18) using a dial connected to it. In this work we tuned the laser light to a wavelength of about 831 nm. The tuned laser light is emitted through the semi transparent mirror and hit the prism (P1) where the beam undergoes total internal reflection. The totally internally reflected beam from P1 is amplified by the amplifier before hitting the prism (P2). After P2 the totally internally reflected laser light passes through the lens system (L5-L6) and mirror (M20), and then get combined with other two dye lasers at M12. The three dye laser beams are collimated by the lenses, and merged by an arrangement of dielectric mirrors before they are fed through an aperture into the vacuum chamber.

3.7.1 Tunable dye lasers

The tunable dye laser cavity consist of dye cuvet, back mirror, grating and the tuning mirror shown in figure 3.14. This cavity is known as a Littman cavity [49]. A grating at the grazing incidence is used. The diffraction grating in the Littman cavity serves both as output mirror and tuning element. The tuning mirror is used for adjusting the emission wavelength.

In our experiment we used three dye lasers which were tuned near 671 nm, 610 nm, 831 nm respectively. The light from a dye laser always have a longer wavelength compared to the pumping light, as a consequence of this visible light cannot be achieved if the dye is pumped with the fundamental wavelength (1064 nm) from the Nd:YAG laser. To get tunable light in the visible part of the spectrum from a Nd:YAG pumped dye laser the pumping light has to be frequency-doubled. Therefore our dye lasers are pumped at 14 Hz repetition frequency by the second harmonic (532 nm) of a Spectra-Physics GCR-11 Nd:YAG laser with pulse length of 8 ns.

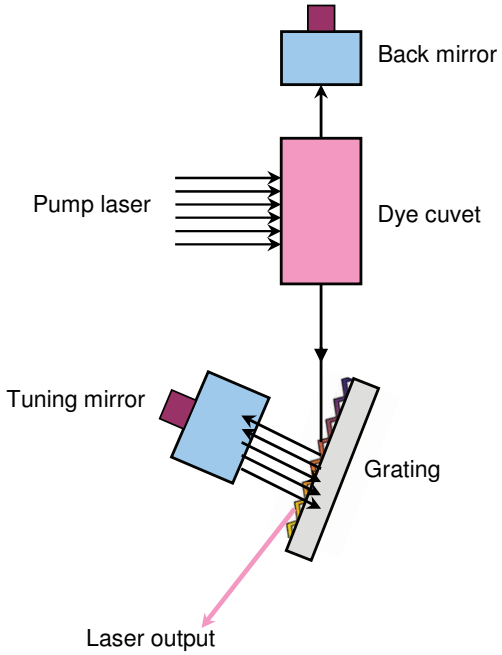

Figure 3.14: Schematic diagram of dye laser cavity.

The first two transitions (2s→2p and 2p→3d) are driven and saturated by two home made dye lasers of the grazing-incidence type [49]. Due to the large oscillator strengths, only about 1 mJ of 532 nm light is needed to pump each of theses lasers. Because of the low power, dye cells are simple unstirred cuvetes loaded with a 4 ml solution of laser dye dissolved in methanol. The laser dyes Rhodamine 640 and Oxazine 720 are used to produce laser light of wavelengths 610 nm and 671 nm respectively. Linewidths of these lasers are estimated to about 10 GHz. The last transition (3d→25f) requires more power and is driven by an old commercial Quantel TDL-III pulsed dye laser, pumped by 50 mJ of 532 nm light [50]. This laser is designed to be pumped by a much higher power, and therefore the original three stage amplification has been reduced to a configuration with only one amplifier. The output power and linewidth obtained are 1 mJ and 6 GHz respectively. From time to time, all three dye solutions has to be replaced because they degrade during operation.

3.7.2 Optimization of the dye lasers

In this thesis work we used the spectrometer USB4000 from Ocean Optics to measure the lasing intensity and florescence of three tunable dye lasers of wavelengths 610 nm, 671 nm and 831 nm. The spectrometer USB4000 is an amazingly compact device which has one input (a fiber optics cable which shines the light into the spectrometer) and a USB port to send data to computer.

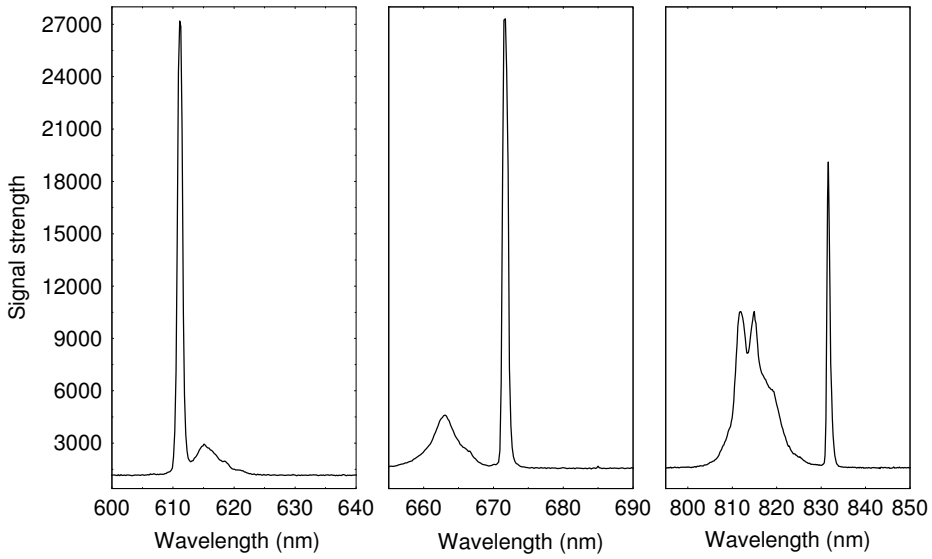

Figure 3.15: a) The laser light of wavelength 610 nm of peak strength 27000 shown in the left side, and with small florescence peak of $\leq$3000 on the right. b) Represents laser light of wavelength 671 nm with peak strength of 27000 on the right and florescence $\leq$5000 on the left. c) Shows laser light of wavelength 831 nm of peak strength $\leq$20000 on the right and florescence $\leq$10000 on the left side. All signal strength are given in relative units.

The software SpectraSuite provided with the spectrometer permits display the spectra. The measured laser lights and fluorescence are shown in the figure 3.15. The spectrometer USB4000 is a very sensitive device, and should not be placed directly into the laser beam. To obtain lasing and florescence for each tunable dye laser we put paper on the lens located next to the laser cavity such that the output laser beam shine on the paper. The fiber optics cable connected to the spectrometer points towards the paper where the laser beam hits. The fiber optics cable leads the light back into the spectrometer. The spectrometer communicates with the computer to convey a real-time display of what it sees [51]. This display is in the form of a graph depicting signal strength vs wavelength (see figure 3.15).

The laser light and florescence shown in figure 3.15 were obtained with one laser at a time while blocking the others. Figure 3.15a shows the 610 nm laser light with peak strength 27000 (relative units (r.u)) on the left with florescence $\leq$3000 (r.u). With this laser we excite Li Rydberg atoms from 2p-3d state. The laser of wavelength 671 nm of peak strength 27000 (r.u) and florescence $\leq$5000 (r.u) is used to excite the Li Rydberg atom from ground state to the first excited state i. e. (2s-2p) is depicted in figure 3.15b. The spectrum shown in figure 3.15c is obtained with the laser light of wavelength 831 nm, with peak strength 20000 (r.u) on the right side along with small florescence peak of $\leq$10000 (r.u) on the left. It excites the Li Rydberg atom from 3d-25f Rydberg level.

3.7.3 Spectral calibration of the dye lasers

Calibration of two dye lasers of wavelength 671 and 610 is performed by the use of a hallow-cathode lamp [52]. This method takes advantage of the fact that the steady state current in a gas filled electrical discharge can be significantly perturbed by resonant radiation. The mechanism is that light induced rearrangement of excited state populations alters the net ionization rate and hereby the impedance of the discharge. The lamp used in calibration of dye is a Ar-filled type with a Li impregnated cathode. It is operated at a current of 10 mA. The lamp system is connected to an oscilloscope. To get lasers on resonance with Li one needs to follow the procedure below:

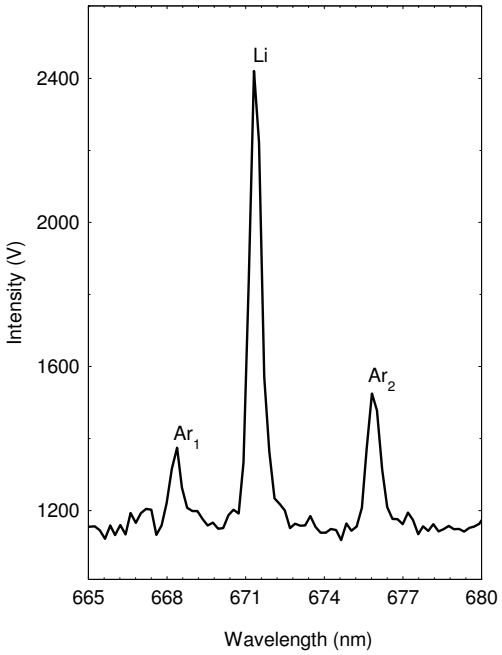

Figure 3.16: Two Ar lines and Li spectra were observed at the same time by the hollow cathode lamp. The values in the plot are the wavelength values of the hollow cathode lamp. They are emitted by the lamp and the signal of the Li increases as the cathode current increases.

- The laser beam is passed through an aperture of 1mm such that only the interior of the hollow cathode is illuminated.
- Two resonance lines in Ar i.e, Ar_1 near 668.4 nm and Ar_2 near 675.8 nm were obtained by tuning the laser light of wavelength 671 nm using micrometer screws connected to the laser cavity (see figure 3.14). The readings on the micrometer for Ar_1 and Ar_2 are l_1=10.6 mm and l_2=17.8 mm respectively. To get the lasers in resonance with Li a calibration value Δl is obtained by using equation 3.6.

$$\frac{\Delta\lambda}{\Delta l} = \frac{\lambda_2 - \lambda_1}{l_2 - l_1} \tag{3.6}$$

where λ_1 and λ_2 are the wavelengths for Ar lines $\mathrm{Ar}_1(l_1)$ and Ar_2 (l_1). And λ is the wavelength of Li impregnated in the lamp where a $\Delta\lambda$ is the difference between the wavelengths of the Li and Ar lines Ar_1 (see figure 3.16).

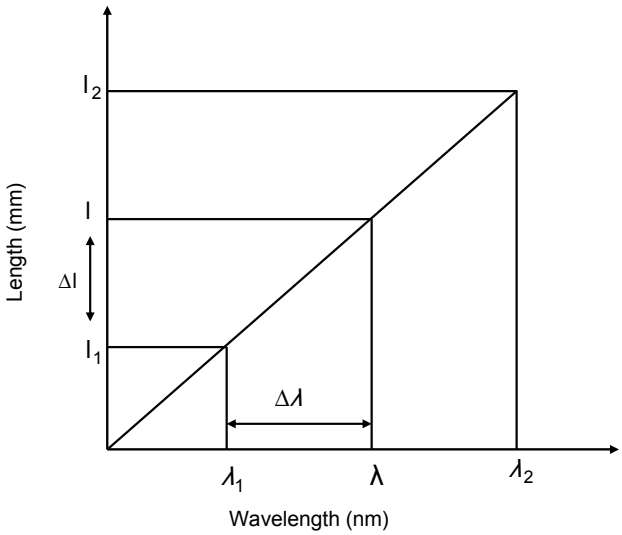

Figure 3.17: Schematic diagram for calibration of dye lasers of wavelength 671nm and 610nm.

- By finding Δl from equation 3.6 one needs to add this value into l_1 to get final value l of the micrometer which correspond to the wavelength (λ) of the Li. This makes 671 nm laser in resonance with Li.
- When the 671 nm laser is in resonance with the 2s-2p transition, a small optogalvanic signal around 2 mV is observed on the digital oscilloscope at 10 mA lamp current.
- Move the micrometer screw attached to laser light of 671 nm little in both directions to maximize the signal strength.
- To adjust two dye lasers to the resonance with Li, the hollow cathode lamp is illuminated with light from both lasers at the same time.
- Put on the laser light of wavelength 610 nm through the aperture of 1 mm and make sure that both of the lasers hit on the interior of hollow cathode lamp in such a way that they must be on top of each other.
- This signal is amplified when second laser is adjusted to resonance with the 2p-3d transition. The 2p-3d resonance could not be observed with the lamp illuminated by 610 nm light alone.
- After getting the maximum signal one should check by blocking the laser cavities for both lasers. If there is no signal by blocking any of the cavity then the lasers are in resonance with Li.

3.8 Blackbody radiations effect on Rydberg target

Rydberg atoms are strongly affected by the blackbody radiation (BBR) even at room temperature. The strong effect of BBR is due to two facts. Firstly, the energy gaps between neighbouring Rydberg levels are small. Secondly, the dipole matrix elements

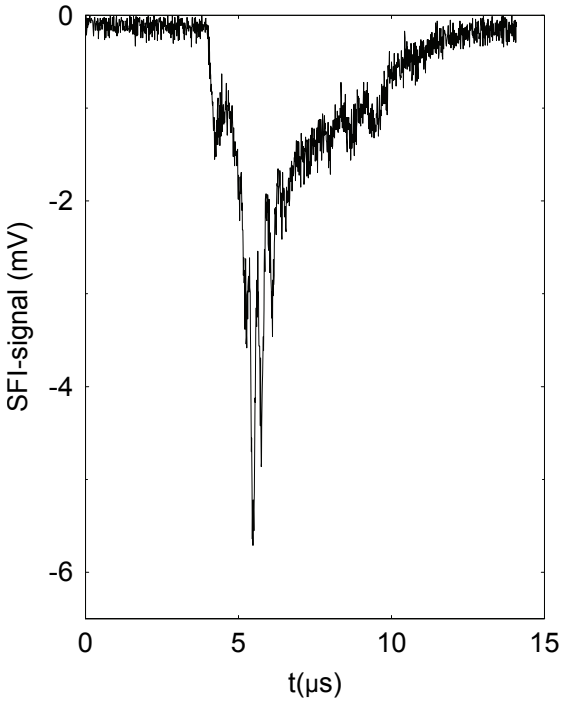

Figure 3.18: Adiabatic spectra recorded by the digital oscilloscope.

for transition between Rydberg states are large, providing excellent coupling to BBR. The result of the strong coupling between the Rydberg atoms and the BBR is that the initial population rapidly diffuses to nearby states unless all parts of the experimental arrangement visible to the Rydberg states are cooled relative to the room temperature.

In our experimental setup all parts of the upper vacuum chamber are mounted in an aluminium cylinder surrounded by a copper shield. Both are attached to a liquid nitrogen bottle so that the Rydberg atoms will be in a cold environment from preparation to detection to reduce the effects of blackbody radiation (BBR). Typical adiabatic SFI-spectra are shown in figure 3.18.

The adiabatic spectrum obtained with the RF-field turned off or not on resonance shows sharp inverted peaks near 6 μs. The deep narrow dip near 6 μs in figure 3.18 shows the spectral position of the circular state $|25,24,0\}$. The smaller dips at later times are due to Stark states of low magnetic quantum (m) belonging to lower energy shells, n=24, 23, 22, 21, ... The intensity at earlier times comes from higher n, the unresolved energy shells. These states are populated by the absorption of black-body radiation by the coherent elliptic state during the travel of approximately 68 μs from

the excitation region to the SFI region. We can limit the blackbody radiation effect on the Rydberg atoms during the excitation and detection process, but obviously can not eliminate it completely, by cooling the apparatus to the temperature of liquid nitrogen [1, 54–58].

3.9 Determination of principal quantum number, n.

Without the Stark field, the infrared laser was tuned into resonance with a number of n shells with tentative assignment n=20 to 37. The resonant wavelengths are listed in table 3.1. The infrared-laser was scanned by the use of the coarse/rough scale with fine scale fixed at 50 and the final value of the wavelength in (nm) is presented in column number three. This wavelength may be off by a constant term due to mechanical

Table 3.1: Measurements and calculations for the assignment of the principal quantum number n to the shell selected for the present work.

Ry=	109737,32	1/cm								
Binding 3d=	12204,05	1/cm							L.Sq. Fit	
n	Measurements			Measurements		Model	n	n-offset=	1,0000	
initial				adjusted			adjusted	lambda_Offset=	0,28559	nm
assignment	IR-laser	IR-laser		IR-laser	IR-laser	IR-laser				
	rough	fine=50.00		wavelength	energy	energy				
n	nf-state	nf-state		nf-state	1/lambda	1/lambda	n	Ratio of	SqDiff	SqSum
	nm	nm		nm	1/cm	1/cm		wavelengths		
37	819,83	824,83		824,54	12127,91	12128,05	38	1,0000	1,96E-02	5,88E-01
36	820,09	825,09		824,80	12124,09	12123,89	37	1,0000	4,01E-02	
35	820,41	825,41		825,12	12119,38	12119,37	36	1,0000	1,77E-04	
34	820,77	825,77		825,48	12114,10	12114,46	35	1,0000	1,33E-01	
33	821,12	826,12		825,83	12108,96	12109,12	34	1,0000	2,30E-02	
32	821,49	826,49		826,20	12103,54	12103,28	33	1,0000	7,08E-02	
31	821,94	826,94		826,65	12096,95	12096,88	32	1,0000	5,45E-03	
30	822,45	827,45		827,16	12089,49	12089,85	31	1,0000	1,29E-01	
29	822,95	827,95		827,66	12082,19	12082,11	30	1,0000	5,92E-03	
28	823,53	828,53		828,24	12073,73	12073,56	29	1,0000	2,89E-02	
27	824,2	829,2		828,91	12063,97	12064,07	28	1,0000	1,05E-02	
26	824,9	829,9		829,61	12053,79	12053,51	27	1,0000	7,77E-02	
25	825,74	830,74		830,45	12041,60	12041,71	26	1,0000	1,24E-02	
24	826,65	831,65		831,36	12028,42	12028,47	25	1,0000	2,09E-03	
23	827,67	832,67		832,38	12013,68	12013,53	24	1,0000	2,29E-02	
22	828,85	833,85		833,56	11996,67	11996,60	23	1,0000	5,09E-03	
21	830,2	835,2		834,91	11977,28	11977,32	22	1,0000	1,56E-03	
20	831,74	836,74		836,45	11955,22	11955,21	21	1,0000	2,75E-04	

Excitation energies of Li I in 1/cm				
		J=3/2	5/2	
NIST:	(1s^2)3d :	31283,08	31283,12	31283,105
	Limit :			43487,15
	(1s^2)3d to			
	Limit :			12204,045

inaccuracies in the control of the mirror angle relative to the grating. This offset is an adjustable parameter determined by a least square fitting procedure. The offset is given in the cell to the right of the one labelled ”lambda-offset”. Column 4 lists adjusted wavelengths and column 5 corresponding energies in units of reciprocal centimetres. In column 6 we show a model calculation of these energies;

$$\frac{1}{\lambda} = I_{3d} - \frac{R_y}{n^2}, \tag{3.7}$$

where I_{3d} is the binding energy of the 3d-state, R_y is the Rydberg unit of energy, and *n* is the adjusted *n*-values shown in column 7. The *n*-offset is shown to the right of the cell labelled "*n*-offset". The measured and adjusted energies in column 5 depend on the "lambda-offset" and the model energies in column 6 on the "*n*-offset". The ratios of the two energies are listed in column 8 and column 9 gives the square difference between them. These are summed in the 10th column, SqSum. A standard least square routine minimizes "SqSum" by variation of either or both parameters in "*n*-offset" and "lambda-offset". A first fit with both parameters free results in "*n*-offset"=1.0042 and "lambda-offset"=0.28859. This unambiguously points at an *n*-offset of 1. A subsequent fit with this parameter fixed leads to the results shown. The binding energy I_{3d} was listed by National Institute of Standards and Technology [59]. The ratios of

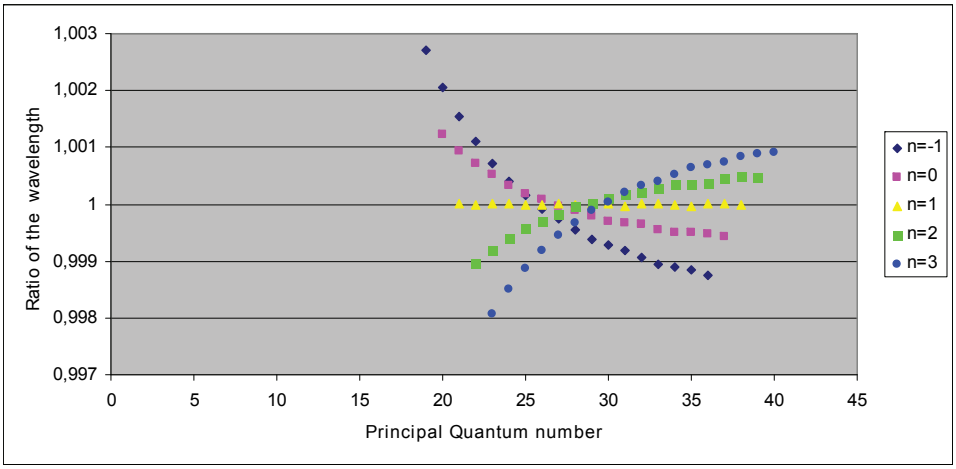

Figure 3.19: Ratio of the wavelength vs tentative principal quantum numbers *n*.

wavelengths for a few values of *n*-offset are shown in figure 3.19 to further illustrate how clearly an *n*-offset different of *n*=1 is singled out and therefore the very high level of certainty by which *n* is assigned.

3.10 Procedure for finding the f, s and *CES* states of *n*=25

We find the f-state by tuning the infrared laser and maximizing the Rydberg target (SFI-signal) without electric and magnetic fields. The different tuning values for the f-state of *n*=25 are listed in table 3.2. Representative data were recorded over a period of two years. With an electric field of 145 V/cm and a B-field of 60 Gauss in the Stark region we then scan down the infrared laser wavelength (up in the energy) until the Stark state correlating with the 26s was obtained (see figure 3.20, upper dot). This state is separated from the rest of the shell in weak fields and is influenced very little by blackbody radiation, so it shows a very sharp and easy to recognize adiabatic SFI signal almost without satellites (at A1 in figure 3.20). The 25 *CES* is then found by tuning down in energy to the next state (at the lower dot in figure 3.20). The 25 *CES*

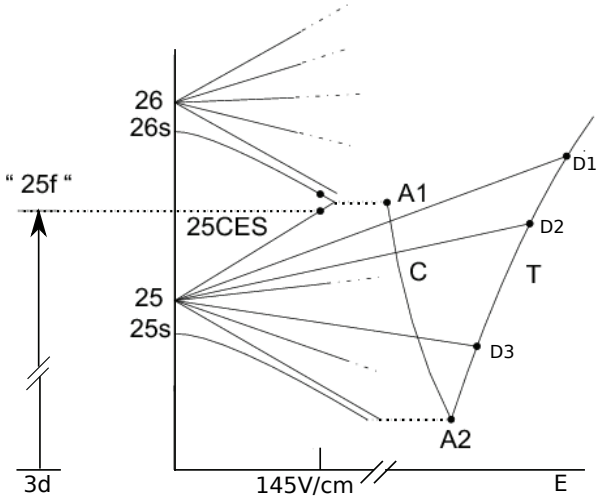

Figure 3.20: Schematic diagram of selected energy levels for n=25-26 in an electric field. Excitation of uppermost n=25 Stark state by the f-character at 145 V/cm. Intershell mixing at E>150 V/cm. The n=25 states with $|m|$<2 show avoided crossings above E>150 V/cm and field ionization at curve C (adiabatic SFI) whereas states with $|m|$>2 are diabatic and they field ionize at curve T (diabatic SFI) [42]. The 25 CES and 26s field ionize adiabatically at A1. Likewise, the 24 CES and 25s field ionize at A_2. The broken straight lines towards A1 and A2 illustrate numerous avoided crossings. A few diabatic states with $|m|$>2 ionizing at D1-D3 are shown.

and 26s both field ionize adiabatically at A_1. Likewise, the 25s and the 24 CES show SFI-signals at A2 and so on.

3.11 Selection of CES and $qCES$ with Fabry-Perot etalon

The infrared laser is normally tuned to excite the uppermost Stark state of maximum polarization quantum number k [1], $|nkm\} = |25,24,0\}$ (coherent elliptic state (CES)), or the degenerate states next to the uppermost state $|nkm\} = |25,23,\pm 1\}$. We refer to them as quasi-coherent elliptic states ($qCES$). The selective excitation of either of these states was facilitated by the use of a Fabry-Perot etalon, which consists of a 5 mm thick plate of glass with two high by reflective surfaces. This is like two semi transparent mirrors separated by a certain distance. The two mirrors will create a standing wave. The F.P will transmit or reflect the light depending on the interference of the standing waves at the mirrors. The Fabry-Perot etalon was used to decrease the band-width of the 831 nm laser from 6 GHz to 3.3 GHz. Selective excitation is possible only when the energy gap between the relevant states, 3.4 GHz at 145 V/cm, is comparable to or larger than the band-width. It was inserted at the exit point of the infrared laser, and adjusted in such a way that maximum laser light passed through it. The signal was maximized

Table 3.2: f and coherent elliptic state (*CES*) for n=25 and 26s

Date	Reading on the fine dial for tuning (units of 0.1 nm)			Reading on the coarse dial (nm)	Final wavelength (nm)		
	f-state	s-state	*CES*		f-state	s-state	*CES*
18.02.09	52.48	56.87	57.63	825.50	830.748	831.187	831.263
04.08.09	52.38	56.60	57.45	825.50	830.738	831.160	831.245
18.08.09	52.40	56.77	57.44	825.50	830.740	831.177	831.244
21.08.09	52.45	56.85	57.55	825.50	830.745	831.185	831.255
07.09.09	52.43	56.70	57.40	825.50	830.743	831.170	831.240
06.10.09	52.44	56.58	57.51	825.50	830.744	831.158	831.251
23.11.09	52.60	56.72	57.70	825.50	830.760	831.172	831.270
15.06.10	52.78	56.50	57.45	825.50	830.778	831.150	831.245
15.09.10	52.50	56.85	57.60	825.50	830.750	831.185	831.260
23.08.10	52.45	56.70	57.45	825.50	830.745	831.170	831.245
08.10.10	52.39	56.87	57.38	825.50	830.739	831.187	831.238
28.11.10	52.40	56.78	57.42	825.50	830.740	831.178	831.242
25.11.10	52.53	56.75	57.45	825.50	830.753	831.175	831.245
08.12.10	52.35	56.65	57.45	825.50	830.735	831.165	831.245
21.03.11	52.58	56.50	57.41	825.50	830.758	831.150	831.241
29.03.11	52.40	56.43	57.38	825.50	830.740	831.143	831.238

by the use of tuning screws attached to it. A DC-field of 145 V/cm and a magnetic field of 60 Gauss were used to lift the degeneracy of n=25 shell. After maximizing the SFI-signal, the measurement was taken by the use of the single experiment LabVIEW program (chapter-4) to acquire SFI data to the disk. With the fixed magnetic field of 60 Gauss and a varying electric field (140 to 151 V/cm) the measurements were taken to find the exact DC-field required to excite the *CES* and *qCES*. For this purpose a number of measurements were taken around 145 V/cm (see figure 3.21). The blue spectrum (with the DC-field of 145 V/cm) was used as a reference or standard spectrum. The *CES* ($|nkm\} = |25,24,0\}$) and *qCES* ($|nkm\} = |25,23,\pm1\}$ marked pink were obtained at 142 V/cm and 148 V/cm respectively when the standard signal reduces to half of its actual value. The *CES* and *qCES* obtained experimentally are comparable with the calculated values presented by Førre et al [34].

3.12 s-states of different n-shells

As explained in the section 5.2 the *n*s and *nCES* states field ionize adiabatically at the same n-dependent field value (A_1, A_2 in figure 3.22). For this reason and because the s-states are the easiest to recognize among all the states of the different shells (due to their sharp SFI spectra). They are good proxies for *nCES* when one wishes to find the field-ionization positions for these *nCES* states. This is important for identifying the extra dips seen in figure 3.18 as satellites formed by blackbody radiation induced transition to neighboring n-shells, and we also use this information later in connection

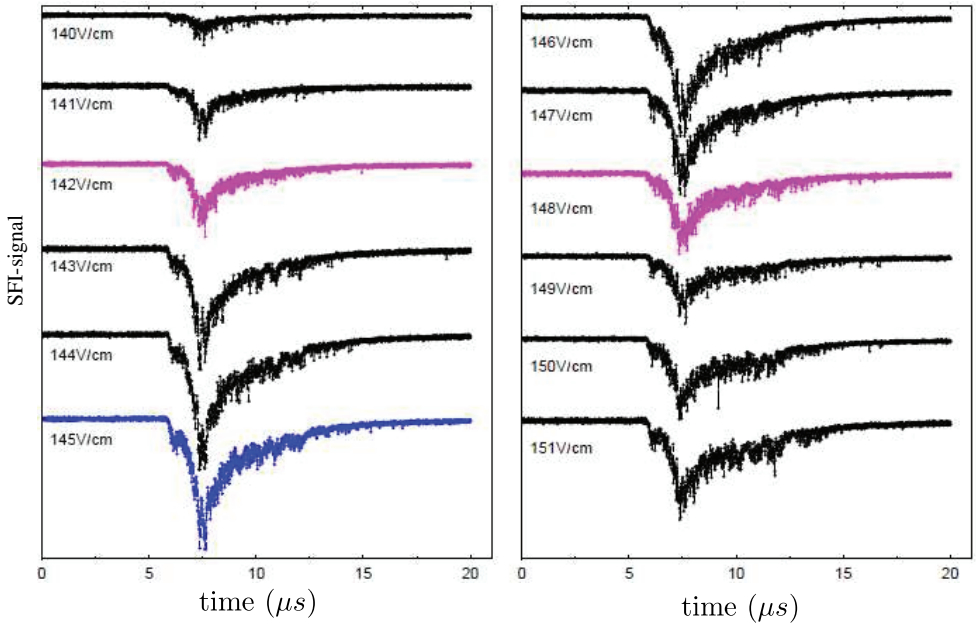

Figure 3.21: SFI-signal vs time (μs) for coherent elliptic states (*CES*) of the selected energy level n=25 for different strengths of the DC electric field.

with the discussion of yet unexplained structures observed in certain reactions. We now present a procedure for finding the s-states for different n-shells. The SFI spectra are depicted in figure 3.22. With the present setup we were able to detect s-states down to n=22 and up to n=26. The lower limit is due to the limitations of the Rydberg target strength which decreases with the increasing wavelengths necessary for exciting states below n=25 (see figure 3.15). The finite strength of the SFI field is also a limiting factor at the lower limit. The upper limit is set by the resolution of the laser, and the increasing density of states as n is increased. To find s-states for different n-shells we

Table 3.3: s-states of different n-shells. Coarse dial setting for 22s was unfortunately lost.

s-states	Wavelength fine dial (0.1nm)	Wavelength coarse dial (nm)	Total Wavelength (nm)	DC-voltage (V/cm)
26s	56.78	825.50	831.178	145V/cm
25s	56.78	826.38	832.058	164.4V/cm
24s	56.78	827.55	834.128	224.0V/cm
23s	56.78	828.77	834.448	250.0V/cm
22s	56.78	-	-	315.0V/cm

start from the 26s-state which is the easiest to see. To find the s-state for the n=25 shell we scan the infrared laser down in energy until the lower limit of n=25 is achieved. After crossing the lower limit of n=25 no signal was found, and the limiting wavelength was recorded. Further scanning down in energy to the upper limit of n=24

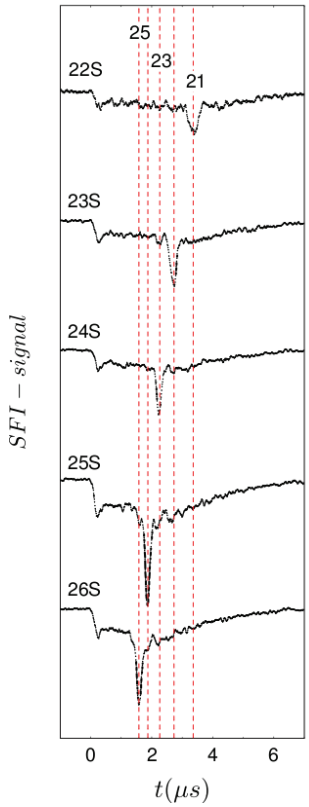

Figure 3.22: The figure show s-states of different energy level for n=22-26.

where the SFI-signal was found, and performed. The corresponding wavelength was recorded. The wavelengths obtained at the lower limit of n=25 and upper limit of n=24 were averaged. The average value of the wavelengths was set by the use of coarse dial, and the DC-field was increased until the avoided crossing for the states with $|m|$<2 was met, and a SFI-spectrum observed. This happens at the Inglis-Teller limit E=$\frac{1}{3n^5}$ [5.14×10^9 V/cm]. The 24 CES and 25s field ionize adiabatically at A2. We then increased the DC-field to a value close to 145 V/cm$\times(26/25)^5$ =176.41 V/cm, and subsequently decreased the wavelength until the s-state correlating with 25s was seen. The same procedure was repeated for finding the other s-states from different shells down to n=22. The different s-states with their corresponding wavelengths (nm) and DC-field (V/cm) are presented in table 3.3.

3.13 Calculation of eccentricities for n=25

The eccentricity, e, of the selected coherent elliptic state and shell splitting is controlled by the orthogonal small external electric (0, E, 0) and magnetic fields (0, 0, B). In the experiments we wish to vary e while keeping the shell splitting ω_{SZ} constant. The

required field values then follow from equations (3.1-3.2). The eccentricities of range 0-1 with corresponding electric, magnetic fields and shell splitting of 95 MHz are listed in the table 3.4.

Table 3.4: Calculation of different eccentricities for n=25 with shell splitting of 95 MHz.

		n=	25,0000	Shell				
		f=	95,0000	MHz				
	e		E	V_DC	V_offset		B	I
			V/cm	V	V		Gauss	A
	0,0000		0,0000	0	0		67,8571	6,000
	0,1000		0,1980	0,099	0,0495		67,5170	5,97
	0,2000		0,3960	0,197999	0,099		66,4862	5,88
	0,3000		0,5940	0,296999	0,148499		64,7316	5,72
	0,4000		0,7920	0,395998	0,197999		62,1921	5,50
	0,4500		0,8910	0,445498	0,222749		60,5984	5,36
	0,5000		0,9900	0,494998	0,247499		58,7660	5,20
	0,5500		1,0890	0,544498	0,272249		56,6719	5,01
	0,6000		1,1880	0,593997	0,296999		54,2857	4,80
	0,6500		1,2870	0,643497	0,321749		51,5670	4,56
	0,7000		1,3860	0,692997	0,346499		48,4597	4,28
	0,7400		1,4652	0,732597	0,366298		45,6412	4,04
	0,7600		1,5048	0,752397	0,376198		44,1019	3,90
	0,7800		1,5444	0,772197	0,386098		42,4636	3,75
	0,8000		1,5840	0,791997	0,395998		40,7143	3,60
	0,8500		1,6830	0,841496	0,420748		35,7460	3,16
	0,9000		1,7820	0,890996	0,445498		29,5782	2,62
	0,9500		1,8810	0,940496	0,470248		21,1884	1,87
	1,0000		1,9800	0,989996	0,494998		0,0000	0,00
e=	0,3	Eccentricity						
				Calibration				
E	B	I						
V/cm	Gauss	A		I(A)=	6			
				B(G)=	67,86			
0,59	64,73	5,72						
				Ratio=	11,31	G/A		
					0,08842	A/G		

3.14 Effect of stray electric field on Rydberg atoms

Rydberg atoms are inherently very sensitive to the external fields. In this experiment, the most critical region is the RF-region, where the cloud of Rydberg atoms interact with a linearly polarized electric field in the presence of orthogonal DC-electric and magnetic fields. A slight deviation from orthogonality of the electric and magnetic fields has an effect similar to a stray field parallel to B. Even a small electric stray field of the order of $\simeq$45 mV/cm will cause measurable effects on the measurements.

In this work, measurements consist of multiphoton resonances. These resonances split because of the stray electric field. A small component, E_{st}^{p}, parallel to the magnetic

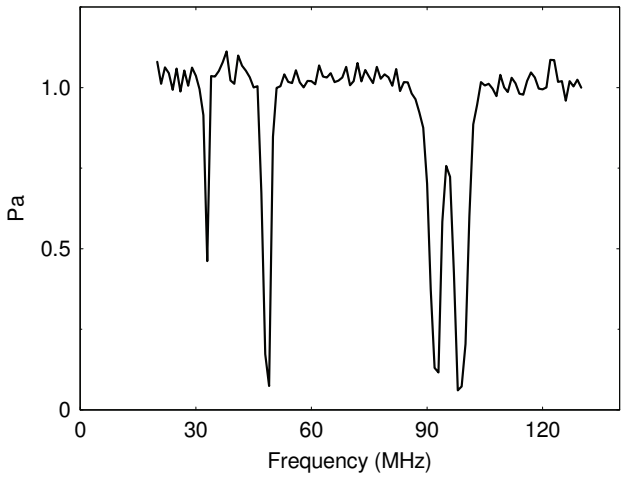

Figure 3.23: Adiabatic probability *Pa* vs frequency f of the harmonic field. N-photon resonances with N=1, 2 and 3 are seen near f=95, 48 and 33 MHz, respectively.

field (B) results in $\omega_{\pm} = \omega_{SZ}(1 \pm \omega_L \omega_{st}^p / \omega_{SZ}^2)$ or a splitting given by;

$$\Delta\omega = 2\omega_L \omega_{st}^p / \omega_{SZ}. \tag{3.8}$$

The splitting vanishes at e=1, and becomes $\Delta\omega = 2\omega_{st}^p = 3nE_{st}^p$ at e=0. The split in the one photon resonance near 95 MHz can be seen in figure 3.23. In this experimental work where we use a vacuum chamber with a hot oven, a beam of thermal alkali atoms and materials at liquid nitrogen temperatures, surface layers of adsorbed molecules inevitably grow, and these give rise to relatively stable stray fields due to spatially varying contact potentials or vacuum levels [60]. Also charging can occur in case of an insulating layer. The observed splitting is stable for days and smallest after cleaning the chamber. We limited the splitting by using stainless steel everywhere and coating it with a layer of antistatic graphite.

3.14.1 Calculation of stray field from experimental data

Experimental data for 1-3 photon resonances of different eccentricities close to 0, where the sensitivity to the stray field is largest, is shown in figure 3.24.

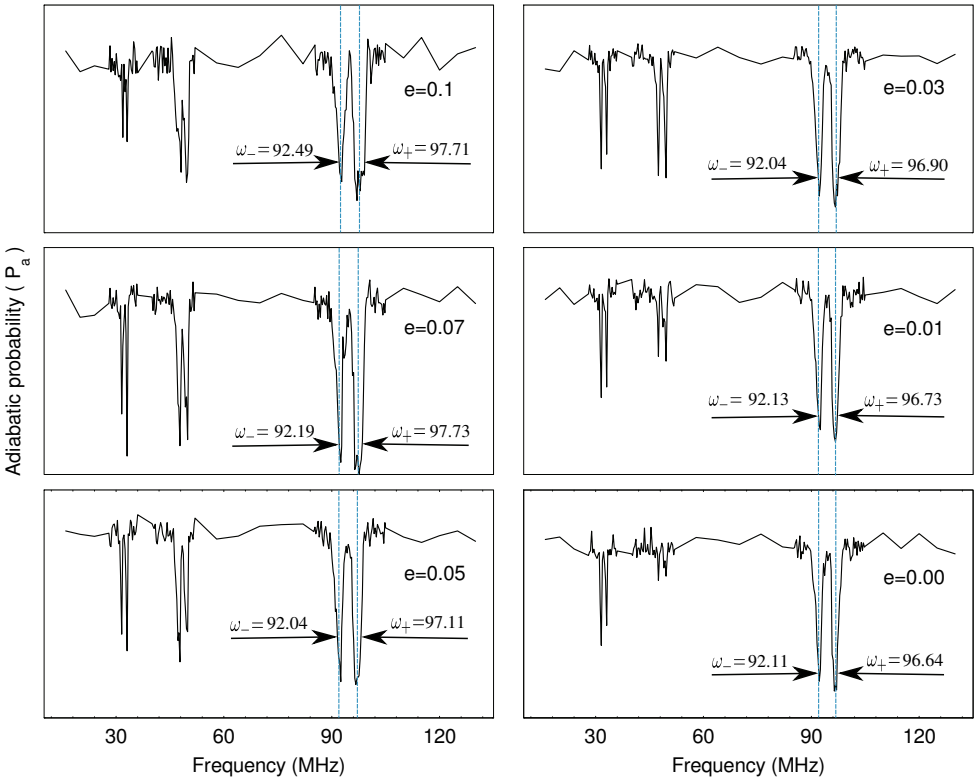

Figure 3.24: Adiabatic probability P_a vs frequency for coherent elliptic states, *CES* of the selected energy level n=25 for different eccentricities.

We observed splitting of N-photon resonances as a function of eccentricities by changing the orthogonal DC-electric and magnetic fields in the RF-region as explained in section 5.5. The splitting is given by equation 3.8 from which the stray field ω_{st}^{p} can be extracted. The results are presented in table 3.5, and shown in the figure 3.25. With the increase of eccentricity (e) the parallel component E_{st}^{p} shows an unexpected

Table 3.5: Calculation of stray field in the one photon region rear 95 MHz.

Eccentricity (e)	$\omega_-/2\pi$ (MHz)	$\omega_+/2\pi$ (MHz)	$\frac{\Delta\omega}{2}/2\pi$ (MHz)	E_{st}^{p} (mV/cm)
0.1	92.49±0.10	97.71±0.10	2.61±0.14	52.2±2.8
0.07	92.19±0.10	97.37±0.10	2.59±0.14	51.8±2.8
0.05	92.04±0.10	97.11±0.10	2.53±0.14	50.7±2.8
0.03	92.04±0.10	96.90±0.10	2.43±0.14	48.6±2.8
0.01	92.13±0.10	96.73±0.10	2.30±0.14	46.0±2.8
0.00	92.11±0.10	96.64±0.10	2.26±0.14	43.5±2.8

increasing trend which is probably not significant. In figure 3.24 one clearly sees that the two photon resonance is suppressed at the smaller eccentricity (e=0), because it

is forbidden by the dipole selection rule. The stray field in (mV/cm) as a function of RF-pulse delay with different RF-pulse widths are plotted and shown in the figure 3.26. The minimum values of the stray field (22.73 mV/cm, 24 mV/cm, 32 mV/cm and 36 mV/cm) are seen near 25 μs, 26 μs and 23 μs with pulse width 1 μs, 1.5 μs, 2.5 μs and 5 μs respectively. The smallest value of the stray field (22.73 mV/cm) was observed for the shortest pulse width of 1 μs and with a pulse delay of 25 μs. The different RF-delays in figure 3.26 correlate with different positions of the Rydberg cloud relative to the RF-plates. At the selected velocity of 2 mm/μs the time range displayed corresponds to a length of 30 mm, the cloud is at the middle of the RF-plates at 32 μs. It is clear from the figure that the stray field increases strongly toward the beginning and the end of the RF-plates.

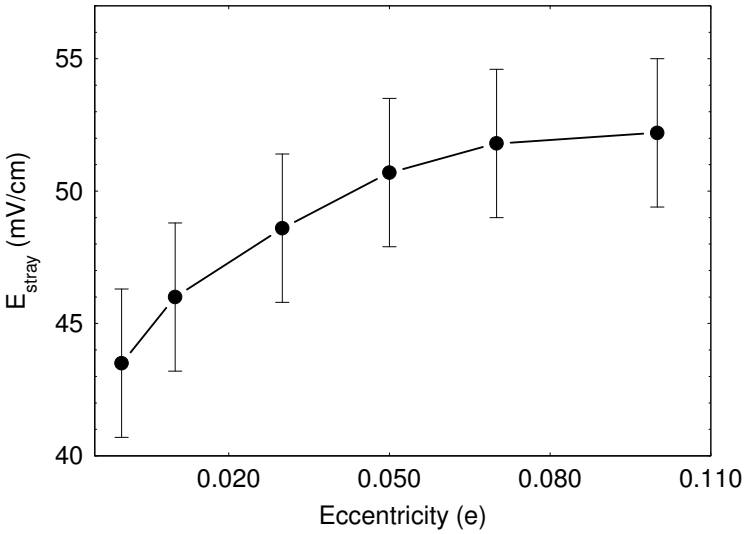

Figure 3.25: Stray field (mV/cm) vs eccentricity (e) for coherent elliptic states, *CES* of the selected energy level n=25.

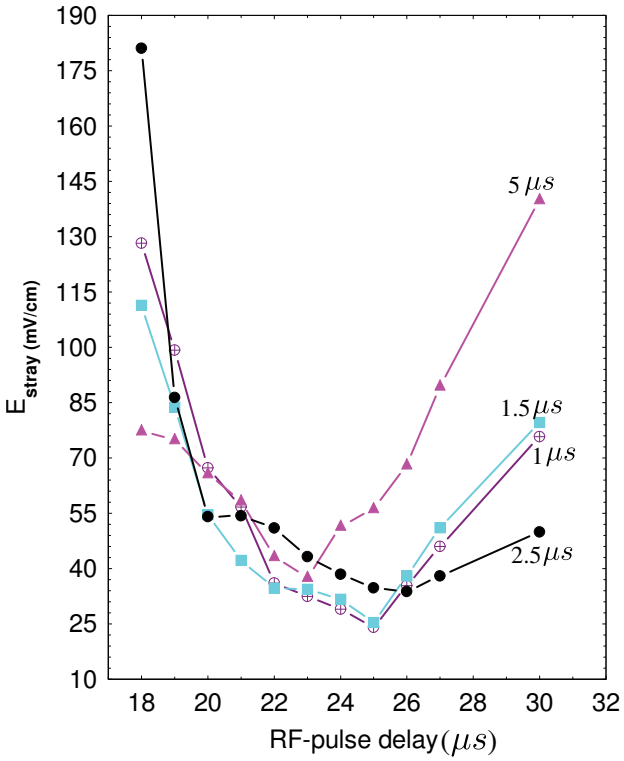

Figure 3.26: Stray field (mV/cm) vs RF-pulse delay (μs) with different RF-pulse width, for coherent elliptic states, *CES* of the selected energy level n=25.

Chapter 4

Computer control of the experiment and data analysis

4.1 The Instrumentation and Data Acquisition System for the Rydberg Experiment

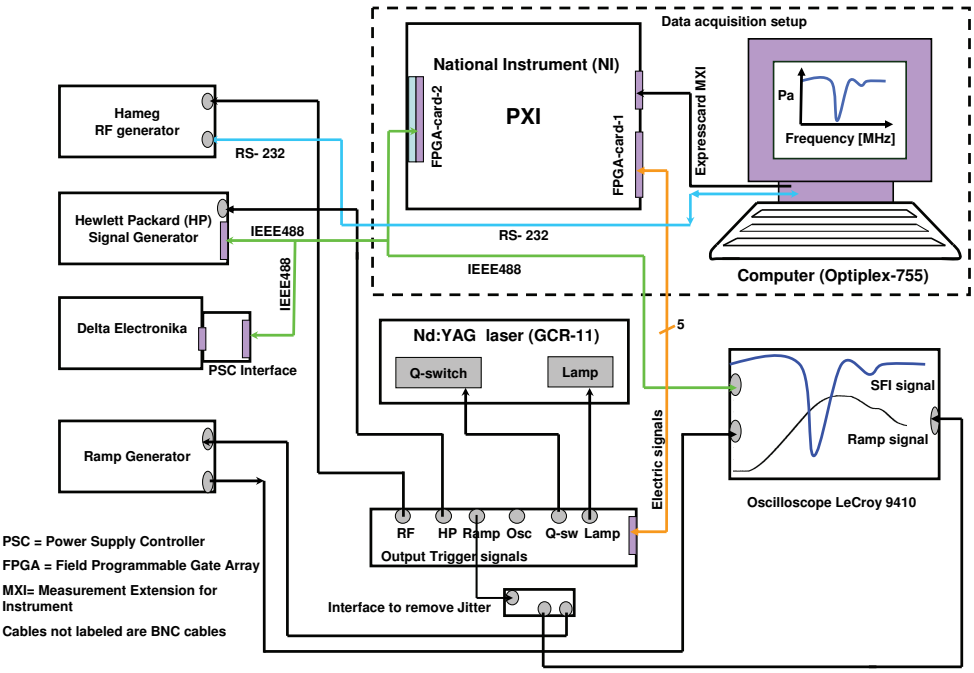

Figure 4.1: Schematic of implemented instrumentation and data acquisition system for the Rydberg experiment.

The instrumentation and data acquisition system for the Rydberg experiment consists of a standard PC controlling and/or acquiring data from a Nd:YAG laser, a Hameg RF (Radio Frequency) synthesizer, a Hewlett Packard signal generator, a Delta

Elektronika power supply, a LeCroy oscilloscope and a high voltage ramp generator using PXI-based (PCI extension for Instrumentation) data acquisition, including IEEE488, GPIB (General Purpose Interface Bus) and RS232 standard instrument interface protocols from the National Instruments (NI). The instrumentation and data acquisition system is programmed using the National Instruments LabVIEW 8.5 software development tool. The instrumentation and data acquisition system serves two main functions:

1. To provide accurate trigger pulses to the different instruments in the experimental setup using PXI FPGA technology.

2. Acquire and store experimental data, i.e. the (Selective Field Ionization) SFI-signal, using the standard IEEE488 and RS232 instrument interface protocols.

A sketch of the implemented instrumentation and data acquisition system for the Rydberg experiment is shown in figure 4.1.

The instruments included in the experimental setup are listed in table 4.1. The Hewlett Packard HP-33120 signal generator, the Delta Elektronika SM 70-22 power supply and the LeCroy 9410 oscilloscope is controlled using the IEEE488 (GPIB) interface protocol. The Hameg HM 8134-2 programmable RF synthesizer is interfaced using the RS232 interface protocol, whereas the functionality of the FP 1019A high voltage ramp generator is voltage controlled. The implemented data acquisition system

Table 4.1: List of main instruments used in Rydberg experiments.

Instrument	Specification
Hameg HM 8134-2	Programmable RF (Radio Frequency) synthesizer -1.2 GHz RS232 interface
Hewlett Packard HP-33120	Function / arbitrary signal generator -15 MHz IEEE488 interface
Delta Elektronika SM 70-22	DC Power supply (0-70 V, 0-22 A) IEEE488 interface
LeCroy 9410	150 MHz -4 GS/s -2 channel oscilloscope IEEE488 interface
Ramp generator FP 1019A	Voltage controlled high voltage ramp generator. The construction of this instrument is based on a design by Fuqua and MacAdam, and is used to generate a linear time dependent electric field in the SFI region

is based on a standard Dell Optiplex 755 PC running the Windows XP operating system, interfacing a 5 slot PXI chassis containing a PXI multifunction RIO (Reconfigurable Input Output) FPGA (Field Programmable Gate Array) card and a PXI GPIB card. The PXI multifunction RIO card is equipped with a 40 MHz Virtex-5 LX30 FPGA, which provides 25 ns IO resolution. The PXI multifunction RIO card generates the trigger signals for the Nd:YAG laser (lamp and Q-switch), the Hameg HM 8134-2 programmable RF synthesizer, the Hewlett Packard HP-33120 signal generator, the LeCroy 9410 oscilloscope and the FP 1019A high voltage ramp generator. The trigger pulse timing is presented later. The PXI GPIB card provides the instrument interface to the Hewlett Packard HP-33120 signal generator, the Delta Elektronika SM 70-22

power supply and the LeCroy 9410 oscilloscope, including experimental readout of the latter, i.e. the SFI signal. The Hameg 8134-2 programmable RF synthesizer is remotely controlled using the RS232 interface protocol available from the Dell Optiplex 755 data acquisition and control PC. For signal conditioning purposes a low power 180 MHz buffer amplifier (EL2002CN instrumentation amplifier) was included at the electrical interface between the high voltage ramp trigger signal output and the high voltage ramp generator input. The components of the data acquisition components are listed in table 4.2.

Table 4.2: List of data acquisition components used in Rydberg experiments.

Component	Specification
Dell Optiplex 755	PC running Windows XP (2.53 GHz Intel Core™ 2 Duo with 1.95 Gbyte RAM)
NI-PXI 1033	National Instruments PXI chassis (5 slots) with integrated MXI-express controller (including PCI remote host card)
NI-PXI 7841R	National Instruments PXI Multifunction RIO (Reconfigurable Input Output) with 40 MHz Virtex-5 LX30 FPGA
NI-PXI GPIB	National Instruments PXI GPIB controller
NI SCB-68	National Instruments shielded I/O connector block for 68-pin connectors (breakout box)
NI LabVIEW 8.5	National Instruments LabVIEW® software development tool version 8.5. LabVIEW is an acronym for Laboratory Virtual Instrumentation Engineering Workbench

4.2 Pulse timing

The trigger pulses for the Nd:YAG laser (lamp and Q-switch), the Hameg radio frequency synthesizer, the Hewlett Packard signal generator, the ramp generator and the LeCroy oscilloscope are all generated by the National Instruments PXI Multifunction RIO (Reconfigurable Input Output), which is equipped with a 40 MHz Virtex-5 LX30 FPGA (Field Programmable Gate Array). This means that a hardware trigger pulse timing resolution of 25 ns can be obtained. Figure 4.2 shows an overview of the timing of the experimental events. The basis for the trigger delay scheme is the 14 Hz lamp trigger signal which is generated by the FPGA card. The lamp trigger pulse is the trigger delay point for the programmable Q-switch trigger delay (pulse width 12.5 μs). The Q-switch pulse is the trigger delay point for the high voltage ramp (pulse width 1.77 ms), the oscilloscope (pulse width 12.5 μs), the RF synthesizer (programmable pulse width) and the HP signal generator (pulse width 12.5 μs). Initially the high voltage ramp and the oscilloscope were triggered with individual FPGA trigger pulses (at different trigger delays). Due to experienced jitter between the high voltage ramp trigger signal and the oscilloscope trigger signal, the high voltage ramp trigger signal was used for both the high voltage ramp and the oscilloscope.

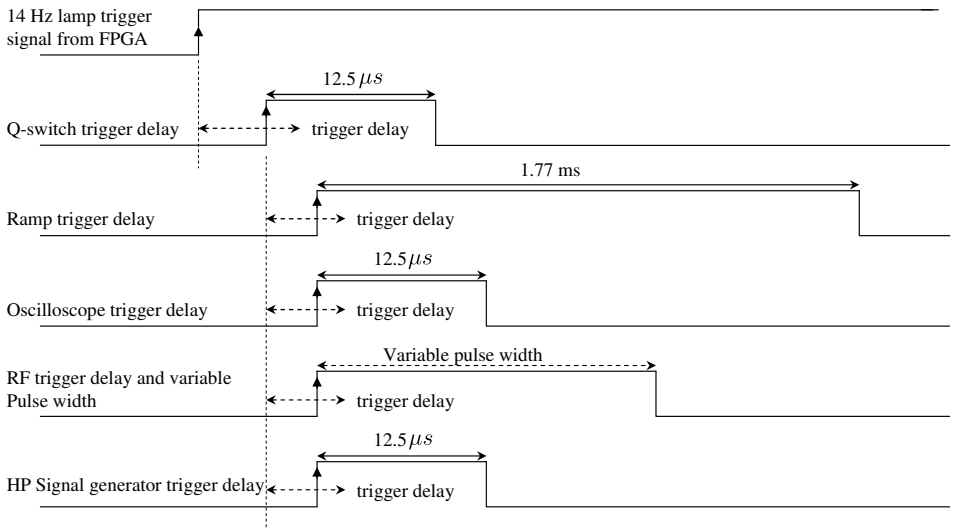

Figure 4.2: Trigger delay timing diagram for the Rydberg experiment. The time axis is not scaled.

4.3 The data acquisition and control software

The data acquisition and control software for the Rydberg experiments is developed using the National Instruments LabVIEW software development tool. LabVIEW programs are called VIs (Virtual Instruments) since they appear similar to a traditional laboratory instrument. Each LabVIEW VI consist of two parts; the front panel and the block diagram. The front panel constitutes the graphical user interface, whereas the block diagram constitutes the actual programming code. The data acquisition and control software for the Rydberg experiments consists of the following three main parts:

1. The main ”Rydberg experiment” LabVIEW program, which facilitates user interaction to:

   i. Configure the trigger signals for the different instruments via the PXI FPGA interface

   ii. Configure the instruments setup via the IEEE488 and RS232 interface protocols

   iii. Select the ”Single” or ”Multiple” LabVIEW program options

2. The ”Single experiment” LabVIEW program. Used to measure a single SFI spectrum.

3. The ”Multiple experiment” LabVIEW program. Used to measure a series of SFI spectra for a user specified range of parameters.

4.4 The main ”Rydberg experiment” LabVIEW program

In the main Rydberg experiment LabVIEW program, the user can individually set the following trigger delay signals:

- Laser Q-Switch Delay
- SFI Ramp delay
- Oscilloscope Trigger Delay
- RF Hameg Trigger Delay
- RF Hameg Pulse Width
- Hp generator Trigger Delay

Furthermore, the LeCroy oscilloscope, the HP 33120 wave generator, the Hameg 8134 wave generator and the Delta Elektronika power supply instruments can be remotely controlled using the IEEE488/RS232 interfaces to alter their default experimental instrument setup. Also, by pressing the control buttons ”Single” or ”Multiple”, the software for running a single or multiple Rydberg experiments, respectively, will be initiated. The single and multiple Rydberg experiment software code is explained next. The block diagram of the main Rydberg experiment LabVIEW program is shown in figure A.1 (see appendix A).

4.4.1 The ”Single experiment” LabVIEW program

The single experiment LabVIEW program allows the user to set the Rydberg experimental parameters, conduct a single experiment and subsequently store the acquired SFI data (ASCII format data file) to disk. In the front panel of the single experiment LabVIEW program, the user can enter the RF frequency (Hameg HM 8134-2), the RF amplitude (Hameg HM 8134-2), the electric current (Delta Elektronika SM 70-22), the number of averaging experimental laser shots, the signal generator amplitude (Hewlett Packard HP-33120) and the signal generator offset (Hewlett Packard HP-33120). The program also allows for a description of the experiment, which subsequently is merged into the acquired SFI data file. The RF pulse delay and pulse width (Hameg HM 8134-2) must be entered in the main Rydberg program. When the experiment has finished, the user is asked to enter a file name to save the experimental SFI data to disk. The format of the SFI data file (ASCII file) is as shown in figure A.3 (see appendix A). The initial part of the SFI data file contains information on the experimental setup, whereas the latter part of the file contains the SFI time series amplitude data output from the LeCroy oscilloscope. The block diagram of the single experiment LabVIEW VI is depicted in figure A.2 (see appendix A).

4.4.2 The ”Multiple experiment” LabVIEW program

The multiple experiment LabVIEW program allows for the experimental parameters to be entered via a MS Excel file using ActiveX software interface programming, i.e.

each row in the MS Excel file will contain the experimental parameters for a single Rydberg experiment. By entering experimental parameters in more than one row of the MS Excel file, multiple Rydberg experiments can be conducted in a very simple manner. As with the single experiment, after each experiment in a multiple experiment sequence, the specific experimental parameters and SFI data is written to disk, as shown in figure A.3 for the Rydberg single experiment LabVIEW program. When running the multiple experiment LabVIEW program, the user has the option of either to enter the experimental data into an MS Excel file via LabVIEW, or alternatively to enter the experimental data into an MS Excel file independent of LabVIEW. The MS Excel file must have the format shown in figure A.5 (see appendix A). The block diagram of the multiple experiment LabVIEW VI is presented in figure A.4 (see appendix A).

4.5 Data analysis

4.5.1 Interpretation of SFI spectra

Typical adiabatic and mixed (adiabatic plus diabatic) SFI-spectra are shown in figure 4.3a. The adiabatic spectrum obtained off resonance (or with RF-field turned off) shows sharp inverted peaks near 68 μs. These correspond to circular Rydberg atoms of n=25 and neighboring shells populated by blackbody radiation.

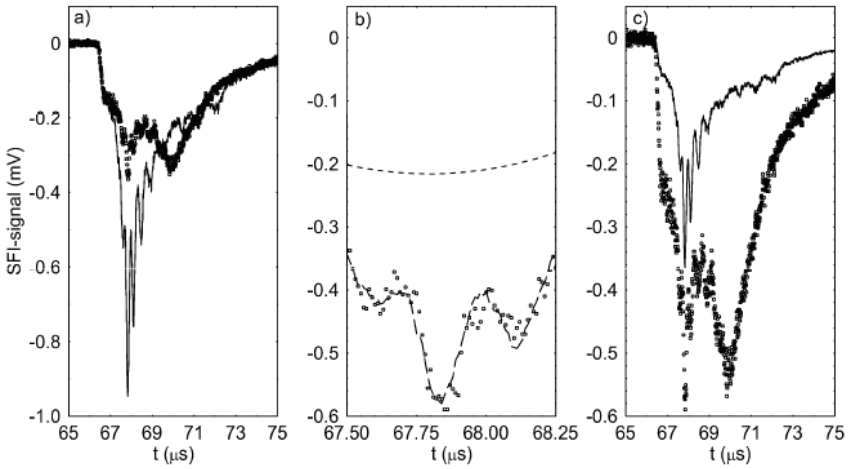

Figure 4.3: Full curves and open points show adiabatic and mixed spectra respectively. a) Spectra as recorded by the digital oscilloscope. b) Adiabatic and mixed spectra fitted to each other in the range of the adiabatic peaks. Short dashed curve, a smooth background. Long dashed curve, adiabatic intensity plus the smooth background. c) Adjusted adiabatic and mixed spectra.

The dominant peak at 68 μs has n=25. Peaks from lower shells (24, 23 $\cdots$) are seen at longer times and peaks from higher shells (26) at shorter times. The mixed spectrum shows sharp adiabatic peaks as well as a broad diabatic distribution coming

from diabatic field ionization by tunnelling (see figure 4.3a). The adiabatic probability P_a, is given by the adiabatic content of the mixed spectrum. This was extracted by fitting the adiabatic spectrum plus a smooth background function in the form of a second-order polynomial to the mixed spectrum. Mathematically this can be formulated as:

$$x_1 + x_2 t_n^n + x_3 t_n^2 + (1 + x_4) V_a(t_n) = (1 - x_4) V_m(t_n) \tag{4.1}$$

where x_1, x_2, x_3 and x_4 are fitting parameters, V_a the adiabatic spectrum, V_m the mixed spectrum, and t_n are the times at which V_a and V_m are measured.

The adjusted spectra $(1 + x_4)V_a$ and $(1 - x_4)V_m$ are shown in figure 4.3c. The fitting was restricted to the region of the adiabatic peaks, and a Linear Least Square Method was used to solve the overdetermined linear system of equations for x_i. This is illustrated in figure 4.3b. The adiabatic fraction is

$$P_a = \frac{(1 + x_4)}{(1 - x_4)} \cdot \frac{\sum_p V_a(t_p)}{\sum_p V_m(t_p)}, \tag{4.2}$$

where each sum extends over the whole spectrum.

4.5.2 The linear least square method

To obtain the adiabatic probability the linear least squares fitting technique was used. It is the simplest and most commonly applied form of linear regression, and provides fit parameters for the best fitting. The method of least squares is a standard approach to the approximate solution of overdetermined system or inexactly specified systems of equations in an approximate sense. Instead of solving the equations exactly, we minimize only the sum of the squares of the residuals. A Matlab program was written for data analysis where linear least square method was applied to find the solution of the overdetermined system (sets of equations in which there are more equations than unknown variables). Equation 4.3 gives the general solution for overdetermined linear system of equations for the unknowns x_i

$$x = (A^T \cdot A)^{-1} \cdot A^T \cdot B, \tag{4.3}$$

where A and B are determined by writing equation 4.1 in the form AX=B.

4.5.3 SFI spectra analysis

A Matlab program was written to extract P_a by using equations (4.1- 4.3). The input data were collected by using a LabVIEW program. The Matlab program requires a number of user defined input parameters. The resulting adiabatic probability depends on the choice made but we show that the dependence is not critical. The parameters are listed below:

i. An " Offset-region"

   It is also called background-region in the SFI-spectrum. To find the adiabatic probability P_a, a DC-offset is subtracted from the adiabatic and mixed spectra. The offset is estimated from the average voltage measured below the actual SFI-spectrum. An example of a selected offset region is shown in figure 4.4. A small

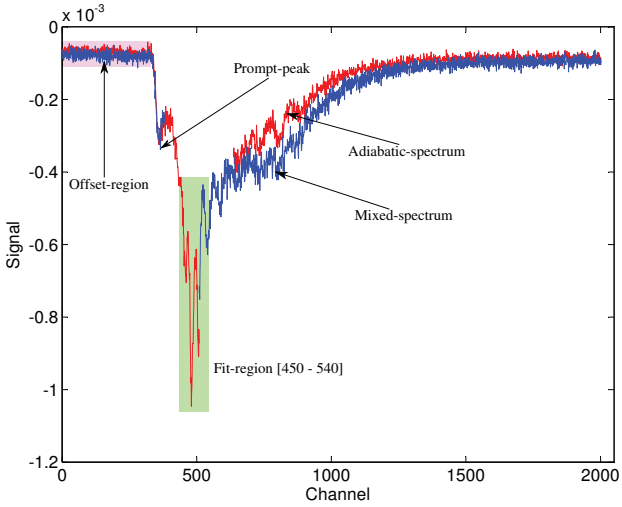

Figure 4.4: SFI-signal in mV vs channel for coherent elliptic state, *CES*, with offset-regions shown (pink) and fit-region from channel number 450-540 marked (green). Mixed and adiabatic spectra are labelled blue and red respectively. The starting point for both adiabatic and mixed spectra is indicated by the prompt-peak.

dip between the end of the offset-region and the fit-region is called the prompt peak. It is the point where adiabatic and mixed spectra start (see figure 4.4).

ii. A ”Fit-region”

It is a region around the n=25 dip. An example comprising the two neighboring shells is shown in figure 4.3b. Another selection including four shells is used in figure 4.4

iii. An ”adiabatic spectrum”

The SFI-spectrum obtained when the Li Rydberg atoms are not in resonance with the applied RF-field. It is formed without intrashell transition from the initial state to the other states within the shell. It is used as a reference spectrum in the data analysis.

iv. A ”Print-spectra”

It is also called mixed spectra, and it is used to judge the quality of the fitting. Figure 4.4 shows an example containing both an adiabatic and a diabatic SFI spectrum.

In the next section we systematically vary the above parameters to show that the adiabatic probabilities are practically independent of the specific choices made for the parameters as long as these are reasonable. As will be seen, broad ranges of parameters lead to the same probabilities within the experimental uncertainties.

Selection of the offset-region

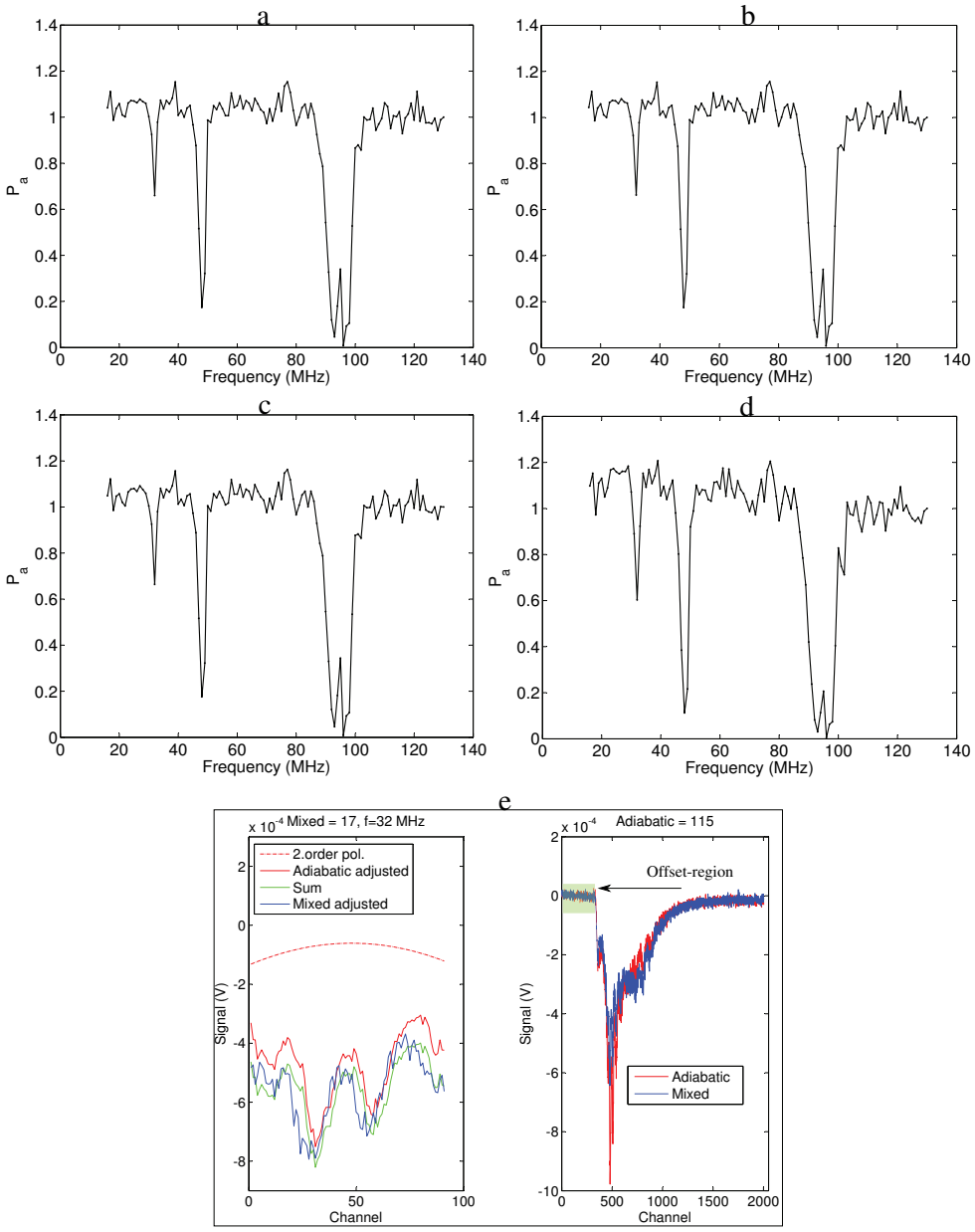

Figure 4.5: Probability P_a vs frequency for coherent elliptic state, *CES*, with varying offset-regions and fixed fit-region, adiabatic spectra and mixed. The offset-regions used are: 1-300, 50-200, 50-300, and 50-450 from 4.4a to d respectively. The offset-region is highlighted green and its upper limit (300) marked by an arrow in the right hand panel of figure 4.5e. Fit-region=450-540, adiabatic-spectrum at 130 MHz and mixed spectrum at 32 MHz are used. Note that the fit region when expanded in the left hand panel starts at channel 0.

The data shown in figure 4.5 was analysed by varying the offset-region within the channel range 1-450. The offset-region highlighted in green has normal channel range 0-300 shown in the right panel of the figure 4.5e. Figures 4.5 (a-d) were obtained by varying the upper and lower limits of the offset-region channel number ranges 1-300, 50-300, 50-200 and 50-450 respectively, with a fixed; fit-region (450-540), adiabatic spectrum at 130 MHz and mixed spectrum at 32 MHz. 1-3 photon resonances are clearly seen in figures 4.5a, 4.5b, 4.5c and 4.5d for frequencies near 96 MHz, 48 MHz and 32 MHz respectively. The results shown in figure 4.5a, 4.5b and 4.5c are almost identical in spite of the varying selection of the offset-regions. The offset-regions used in figures 4.5(a-c) have channel ranges 1-300, 50-300 and 50-200 respectively and all these values lie within the limits of the offset-region. Figure 4.5d looks different from the others in the group because the upper limit that was chosen was beyond the normal offset range selection (0-300). To make changes within the limit of the offset-region will not effect the final result. However the selection of the offset-region that is beyond its channel range will obviously make a difference in the data analysis. From figure 4.5d it is clear that the data analysis is dependent on a reasonable choice of offset region.

Selection of Fit-region

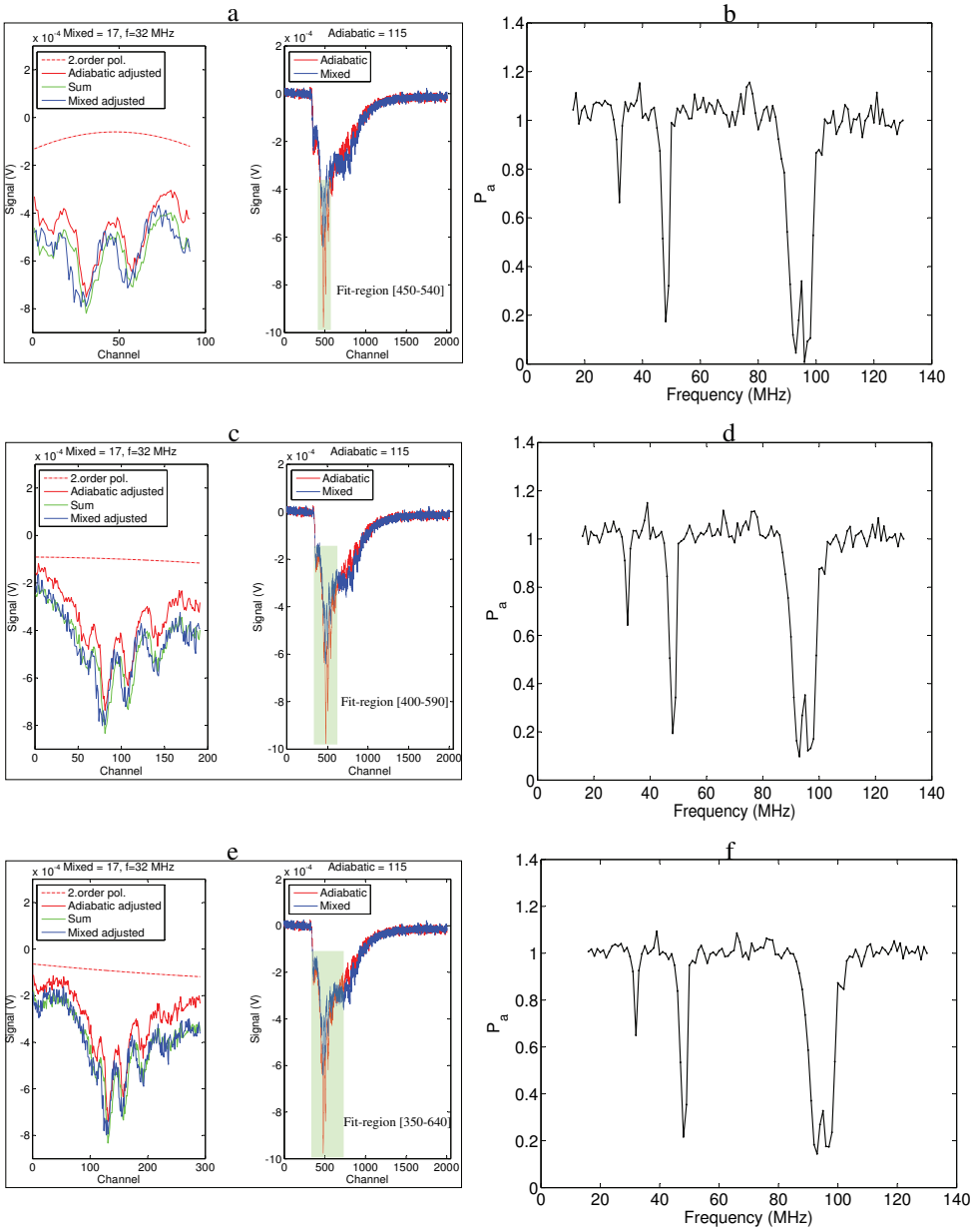

Figure 4.6: Adiabatic probability P_a vs frequency for coherent elliptic state, *CES*, in the right panel and in the left panel signal (V) vs channel numbers are plotted with varying fit-region and fixed offset-region (50-300), adiabatic spectra at 130 MHZ, and mixed spectra at 32 MHZ. The fit-regions used are: 450-540, 400-590 and 350-640.

The results shown in figure 4.6 were obtained by varying the fit regions (highlighted in green) while keeping the other parameters fixed (offset-region, adiabatic spectrum and mixed spectrum). The mixed spectrum measured at 32 MHz corresponds to maximum 3-photon excitation as in the previous figure. Figure 4.6a and 4.6b were obtained by selecting a narrow fit-region (channels 450-540, see right panel of figure 4.6a). The left panel of figure 4.6a consist of background (dotted red), adiabatic adjusted (full curve red), sum (green) and mixed adjusted spectrum (blue). The the spectrum called "sum" is obtained by adding up the adiabatic adjusted and the background/offset-region. In a good fit, the green and blue spectra must follow each other. Figure 4.6c and 4.6d were generated with a broad fit-region (channels 400-590) as seen in the right panel of figure 4.6c. An even broaden range (channels 350-640) was selected in figure 4.6e and 4.6f. Final result of data analysis is presented in figures 4.6b, 4.6d and 4.6f where 1, 2 and 3 photon resonances are seen near frequencies 96 MHz, 48 MHz and 32 MHz respectively. The data shown in the figures 4.6b, 4.6d and 4.6f looks exactly the same for the narrow and much broaden selected range of the fit-region. From the figure 4.6b, 4.6d and 4.6f one can conclude that data analysis does not depend much on the selection of the fit-region.

Selection of adiabatic spectra

An adiabatic SFI spectrum is used as a reference spectrum in the data analysis. It is formed when there are no transitions from the initial *CES* to the other states within the shell. Adiabatic spectra are highlighted green, and shown in figure 4.7.

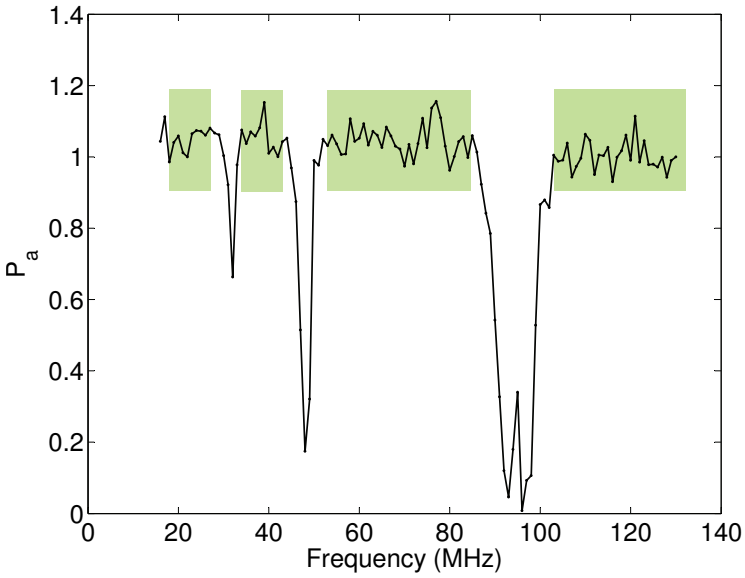

Figure 4.7: Adiabatic probability P_a vs frequency for coherent elliptic state, *CES*, with the adiabatic spectra highlighted (green) and the spectra lie on the dips of one two and three photon resonances near the frequency 96 MHz, 48 MHz and 32 MHz respectively are diabatic.

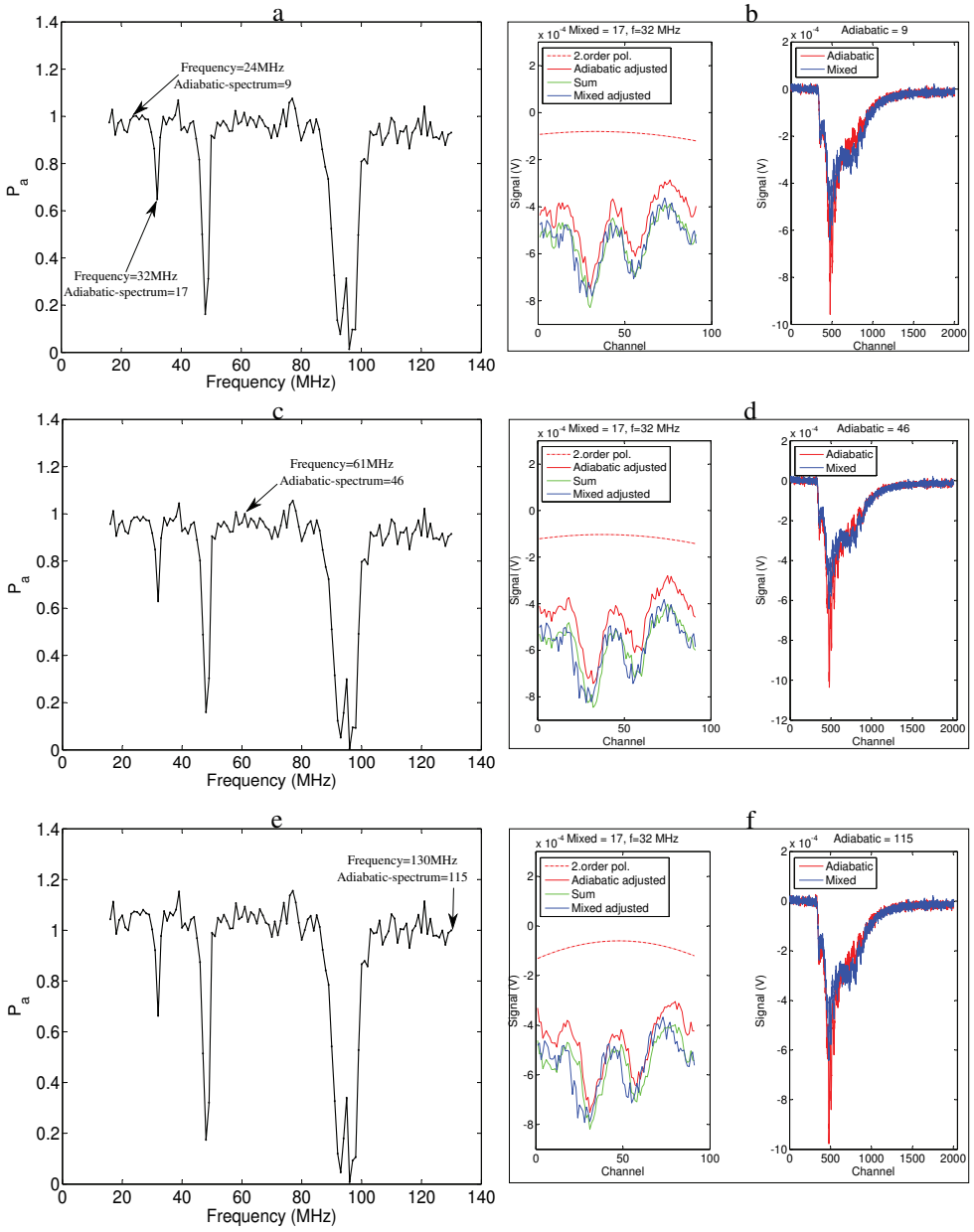

Figure 4.8: Adiabatic probability P_a vs frequency for coherent elliptic state, *CES*, in the left hand panel. The right hand panels show SFI spectra, with the selection of different adiabatic spectra and the same mixed spectrum, fit-region and offset-region. The adiabatic spectra used are: 9, 46 and 115. mixed spectra=17, Offset-region 50-300 and fit-region 450-540.

To find the dependence of data analysis on the selection of adiabatic spectrum, we selected different adiabatic spectra. The adiabatic spectrum selected are: 9, 46, and 115

with corresponding frequencies 24, 61, 130 MHz where no resonance can be seen as shown in the left panel of figure 4.8(a-e).

To judge also the quality of the fitting we used the mixed. SFI spectrum number 17 at the 3-photon resonance as an example. The selection of adiabatic spectra produces the output shown in the right panels of figure 4.8. The selection of different adiabatic spectra does not have an effect on the final results.

SFI-spectrum used to judge the quality of the fitting

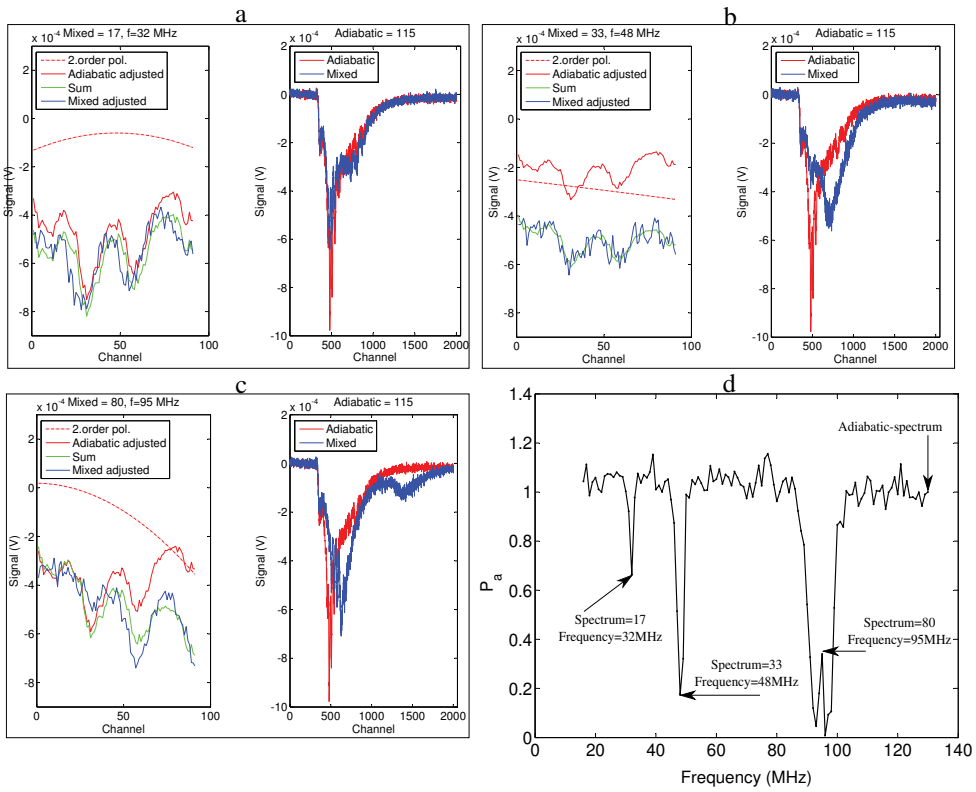

Figure 4.9: Adiabatic probability P_a vs frequency for coherent elliptic state, *CES*, in d, and from a-c SFI-signals. Fixed fit-region, offset-region, and adiabatic spectrum. The mixed spectra used are: 17, 33 and 80 from a to c respectively. Offset-region 50-300, fit-region 450-540 and adiabatic spectra=115.

To check the quality of the fitting for various mixed spectra, different mixed and a fixed adiabatic spectra were used, and the results obtained are shown in figure 4.9(a-c). The SFI-Spectrum number 115 was selected for the adiabatic spectrum. This is located at the end of one photon resonance corresponding to a frequency of 130 MHz (see figure 4.9d). The mixed spectra used are: 17, 33, and 80 with corresponding frequencies 32, 48, 95 MHz respectively (see figure 4.9d). Figure 4.9a was obtained

at the tip of the three photon resonance of frequency 32 MHz. On the left of the window of figure 4.9a we see that the green and the blue curves nicely follow each other. When the spectrum number 33 was selected for a mixed spectrum the fitting looked different compared to spectrum 17 as seen in figure 4.9b, but the fitting is still satisfactory. Figure 4.9c was generated when the spectrum number 80 (at the middle of the one photon resonance) was selected as mixed spectrum (see figure 4.9d). Adiabatic and mixed spectra in the right of the window for figure 4.9c can be distinguished very clearly. The final results consist of mutiphoton resonance shown in figure 4.9d. The selection of different mixed spectra apparently have no significant effect on the final results.

Chapter 5

Introduction to papers

The main part of this thesis is allocated to the experimental studies of the dynamics of highly excited Rydberg states in orthogonal electric and magnetic fields. This thesis consists of 5 papers. The first four papers contain experimental work in which intrashell dynamics of Li Rydberg atoms were studied. The papers are all written in collaboration with 2-8 co-workers, which I have worked with during my PhD project. My contribution to first four papers has been the experimental work in the laboratory for performing the measurements, participated in interpretation of the data and writing the papers and contributing to the discussions. The fifth paper contains the theoretical work about the visualization and studies of Rydberg states. In this paper I participated in developing Matlab code for visualization and studies of Rydberg states, in addition to assisting in writing the paper.

Paper I: Symmetry and symmetry breaking in Rydberg-atom in intrashell dynamics

The objective of this paper is to study two-level interference dynamics in alkali Rydberg atoms. We have studied both experimentally and theoretically the n=25 intrashell dynamics of lithium Rydberg atoms subjected to both a slowly varying and a rotating electric field. The Rydberg atoms were initially prepared in the $|nkm\} = |25, 23, \pm 1\}$ Stark states in the presence of a strong constant electric field. All external fields in the experiment were sufficiently weak and the time dependences slow enough that the dynamics was restricted to the given n=25 shell. Regular oscillatory interference structures were observed in the transition probabilities, and it was shown from theoretical calculations that the nonhydrogenic core of lithium is essential in explaining the underlying dynamics. Furthermore, the theoretical calculations revealed that the nonhydrogenic dynamics of the full system can be reduced to the dynamics of a two-level system. In this particular case by inspecting the two-level dynamics we were able to uncover the interference mechanisms responsible for the observed oscillations in the spectra. The resulting two-level dynamics could be controlled by varying the field parameters in the experiment. Thus, the present alkali-metal Rydberg system represents a controllable two-level system. The present study is an example of the dramatic and selective influence even a small deviation from perfect symmetry may have on a system. When $e \simeq 0$ in the interaction region the dynamics is highly regular and described accurately in terms of hydrogenic theory independent of the initial state [31, 34], whereas if $e \simeq 1$ even neighboring states may behave completely differently as a result of the symmetry breaking scattering off the core.

Paper II: Suppression of multi-photon intrashell resonances in Li Rydberg atoms

In this paper we investigate the suppression of multiphoton intrashell resonances in Li Rydberg atoms. The object of this paper is to investigate the problem of multiphoton suppressions, studying intrashell multiphoton resonances in Li(n=25) Rydberg atoms, perturbed by orthogonal electric and magnetic DC-fields and a pulsed, time-harmonic electric field linearly polarized in the direction of the DC electric field. The atoms are initially prepared in even mixtures of *CESs* and quasi-coherent elliptic states (*qCESs*) of given eccentricity e. Suppressions of N-photon resonances, with N=1-9, are observed at specific values of the eccentricity of the initial state, depending on the order of the multiphoton resonance.

In some cases the suppression are anticipated either because of dipole selection rules (at e=0 for even photon numbers) or because the initial state is an eigenstate of the full (time-dependent) Hamiltonian (at e=1). In other cases (at $e\neq0$ or 1 and N$\geq$3) suppression can be interpreted due to destructive interference between different amplitudes contributing to the resonance in perturbation theory [20], but the suppression are also seen at strong fields.

Paper III: Unidentified transitions in one-photon intrashell dynamics in Rydberg atoms

In this paper we studied experimentally the intrashell dynamics of strongly driven Li(n=25) atoms in the region of their one-photon resonance. The degeneracy of the n-shell is removed placing the atoms in orthogonal DC electric and magnetic fields, defining the eccentricity of the initial coherent elliptic state (*CES*). The atoms are initially prepared in coherent elliptic states of a given eccentricity, in perpendicular DC electric and magnetic fields, and are then exposed to a linearly polarized radio-frequency (RF) pulse. The RF field is pointing along the major axis of the ellipse, defined by the quantum state. Furthermore, the magnetic field is perpendicular to the elliptic plane, and the DC electric field is aligned with the RF field. The static electric and magnetic fields lift the degeneracy of the n-shell giving rise to one- and multiphoton transitions when a multiple of the RF frequency is near resonance with the Stark-Zeeman splitting of the shell. A small DC component of the electric field parallel with the magnetic field splits the one-photon resonance into two, and the dynamics in the intermediate region is studied in detail using state-selective field ionization (SFI). Characteristic structures in the SFI spectra are found and investigated systematically by varying the RF pulse duration and intensity, and for initial states of different eccentricities. Unexpected modulations in the SFI spectra are found and analysed in detail.

Paper IV: Intrashell RF-resonances in Li Rydberg atoms. Linear polarization and unexplained spectral features

In this paper we present experiments and theory for multiphoton intrashell dynamics of Li(n = 25) Rydberg atoms driven by pulses of linearly polarized, time harmonic fields in the radio frequency (RF) region and covering a broad range of strengths. The atoms were initially prepared in a *CES* of given eccentricity determined by constant electric and magnetic fields orthogonal to each other, and the linear polarization was in the

direction of the major axis of the *CES*. Atoms with an electron in a *qCES* or with equal mixtures of *CES* and *qCES* were also formed. The constant fields partially remove the degeneracy of the *n*-shell and gave rise to a Stark-Zeeman energy splitting of the shell. N photon resonances with N =1-6 were observed and confirmed by simulations and a significant broadening of the one-and two-photon resonances was seen in the strong field limit. The broadening of the split one-photon resonance is peculiar. According to the calculations with quantum defects, the downshifted resonance broadens only toward lower frequencies and the upshifted one only toward higher, while the system exhibits a remarkable stability against excitation in between the two. These trends are confirmed by the experimental results but differences exist in the detailed shapes of the resonances, and while theory predicts stability between the split one-photon resonances the experimental results reveal strong transitions but apparently of a different nature than the ones at the resonances.

Paper V: Visualization and studies of Rydberg states

An approach to visualization and interpretation of theoretical results for Rydberg states is presented in this paper. For many purposes it is important to have an easily understandable and accurate picture of the atomic states. This is especially true for the highly excited states which exhibit very complex features not present in the well known states hydrogen-like orbitals with usual lower values of the quantum numbers. In this paper we discuss the problems, review some less fortunate earlier presentations and propose guidelines for applications. Special attention is given to the so called Stark states and coherent elliptic states of Rydberg atoms. We also present a new graphical analysis of the eigenstates in combined electric and magnetic fields with arbitrary geometrical configurations.

Chapter 6

Conclusion and future work

An experimental arrangement (described in section 3.3 & 3.4) for studying Rydberg atoms in nano- and femto-second laser fields has recently been implemented. The first goal was to make this arrangement (vacuum chamber) operational, and ensure that its functionality is properly understood and controlled. This has not been a trivial task. First the lasers had to be set up and aligned. The operation of the commercial (but strongly modified) and the two home-built dye lasers is difficult requiring a thorough knowledge of the working principle of dye lasers as well as considerable practical experience built up from daily work in the lab. The new vacuum system with an untested arrangement of electrodes, a new oven for the thermal beam of Li-atoms, and a new arrangement of detectors also created many problems which had to be identified and solved.

A large proportion of this thesis is devoted to a thorough description of the apparatus reflecting the considerable effort invested in understanding and controlling the experimental arrangement. The scientific work has been concentrated on nanosecond lasers to excite coherent elliptic Rydberg states of Li atoms, and the study of intrashell dynamics of Rydberg atoms with *CES* as initial states. The *CES* were formed by laser excitation in orthogonal electric and magnetic DC-fields and the intrashell transitions were driven by a pulsed, time-harmonic RF electric field. The RF-field was linearly polarized in the direction of the DC-fields. To highlight a few scientific results of the work we mention three of them:

Firstly, the effect on the intrashell dynamics of the symmetry breaking by the non-hydrogenic core of Li is described in paper I. Even though only a few states in the shell are affected the influence may be dramatic. In this case it leads to a series of regular oscillations of transition probabilities which can not be understood by a hydrogenic model.

Secondly, the suppression of multiphoton intrashell resonances was examined in paper II. In contrast to the above effect, the most interesting suppressions are hydrogenic in nature, and they depend on the full dynamic symmetry of a hydrogenic atom. This type of suppression was first observed and discussed by Yabuzaki et al [61, 62], in relation to optical pumping of a Cs vapour in a magnetic field with a constant and a time-harmonic component. The optical two-level system can be represented by a spin-1/2 system in the same fields. The suppression occurs at specific angles between the fields. Due to the Majorana reduction of a general spin system to a spin-1/2 system the results apply also to intrashell transitions in Rydberg atoms.

A predicted systematic increase in the number of suppression angles with increasing multiphoton order N was tested by Yabuzaki et al [61, 62] only for some low N-values. We were able to extend this to significantly higher orders, and at the same time test the predictions for a completely different physical system.

Thirdly, SFI-spectra of unusual character and shape were observed between split one-photon resonances. The SFI spectra obtained when intrashell transitions out of the initial CES are present normally consist of a few adiabatic lines at low SFI field values followed by a broad structureless distribution of diabatic ionization channels at larger fields. This pattern is dramatically broken for split one-photon resonances when certain extra conditions on the RF-field strength and the eccentricity of the CES or ($qCES$) are met. The broad diabatic distribution is replaced by a number at discrete lines, which at first sight might look like adiabatic lines from different neighboring shells. However a test of this hypothesis was not conclusive, and a mechanism for effectively transferring the population to other shells under these special conditions has not been found so far, although some speculation has been made. The quantum mechanical model used successfully to interpret all other aspects of intrashell transitions as observed until now does not provide a solution to the problem, so in this respect the presence of these discrete lines is perhaps the most interesting result obtained by the new experiments since it appears that an unexpected mechanism is at work.

In the laboratory we also have access to a femtosecond laser. A natural continuation of this research would be to incorporate this laser in the experiments on the Rydberg states. For example the studies of wave packet of the intershell dynamics. A study of this type of dynamics could be implemented by starting from $3d$ state. The dynamics of Rydberg wavepackets will be studied in external electric and magnetic fields. The final quantum state will be detected and analyzed by a combination of selective field ionization and pulse/probe techniques.

Bibliography

[1] T. F. Gallagher, Rydberg Atoms, University Press, Cambridge (1994) 1, 1, 2.1, 2.3.1, 3.3.1, 3.3.3, 3.4, 3.5, 3.5, 3.5, 3.8, 3.11

[2] L. Nyvang, D. Fregenal, M. Førre, and E. Horsdal-Pedersen, J. Phys. B **37**, 4039 (2004) 1

[3] K. S. Mogensen, J. C. Day, T. Ehrenreich, E. Horsdal-Pedersen and K. Taulbjerg, Phys. Rev. A, **51**, 4038 (1995) 1, 1

[4] L. Kristensen, E. Horsdal-Pedersen and P. Sørensen, J. Phys. B, **31**, 1049 (1998) 1

[5] P. Sørensen, J. C. Day, B. D. DePaola, T. Ehrenreich, E. Horsdal-Pedersen and L. Kristensen, J. Phys. B, **32**, 1207 (1999) 1

[6] D. Fregenal, T. Ehrenreich, B. Henningsen, E. Horsdal-Pedersen, L. Nyvang and V. N. Ostrovsky, Phys. Rev. Lett, **87**, 223001 (2001) 1

[7] D. Fregenal, M. Førre, E. Horsdal-Pedersen, C. Fisker and N. AKjar. J. Phys. B, **41**, 105003 (2008) 1

[8] I. Pilskog, D. Fregenal, O. Frette M. Førre, E. Horsdal and A. Waheed, Phys. Rev. A, **83**, 041806 (2011) 1

[9] A. Waheed, D. Fregenal, Ø. Frette, M. Førre, B. T. Hjertaker E. Horsdal, I. Pilskog, and J. Preclíková, Phys. Rev. A, **83**, 063421 (2011) 1, 2.1, 3.3.2

[10] J. Hare, M. Gross, and P. Goy, Phys. Rev. Lett, **61**, 1938 (1988) 1

[11] D. Delande and J. C. Goy, Europhys. Lett, **5**, 303 (1988) 1, 2.1

[12] N. Bohr, Philosophical Magazine, **26**, 1 (1913) 1

[13] E. Schrödinger, Phys. Rev, **28**, 1049 (1926) 1

[14] E. Schrödinger, Naturwissenshaften, **4**, 664 (1926) 1

[15] E. Schrödinger, Naturwissenshaften, **14**, 137 (1926) 1

[16] W. Heisenberg, Z. Phys. 43, 172 (1927) 1

[17] R. F. Stebbing, and F. B. Dunning, in Rydberg States of Atoms and Molecules, University Press, Cambridge (1983) 1

[18] J. C. Day, T. Ehrenreich, S. B. Hansen, E. Horsdal-Pedersen K. S. Mogensen, and K. Taulbjerg, Phys. Rev. Lett A, **72**, 1612 (1994) 1, 2.1, 2.1

[19] D. Fregenal, E. Horsdal-Pedersen, L. B. Madsen, M. Førre, J. P. Hansen and V. N. Ostrovsky, Phys. Rev. A, **69**, 031401(R) (2001) 1

[20] D. Fregenal, M. Førre, B. Henningsen, E. Horsdal and D. Richards, Phys. Rev. A, **76**, 053414 (2007) 1

[21] M. Førre, D. Fregenal, J. C. Day, T. Ehrenreich, J. P. Hansen, B. Henningsen, E. Horsdal-Pedersen, L. Nyvang, O. E. Povlsen, K.Taulbjerg and I. Vogelius, J. Phys. B, **35**, 401 (2002) 1, 2.3.1

[22] R. G. Hulet and D. Kleppner, Phys. Rev. Lett, **51**, 1430 (1983) 2.1

[23] J. Liang, M. Gross, P. Goy and S. Haroche, Phys. Rev. A, **33**, 4437 (1986) 2.1

[24] A. Bommier, D. Delande and J. C. Gay, Atoms in Field, edited by C. A. Nicolaides et all, Plenum Press (1990) 2.2.1

[25] C. Lena , D. Delande and J. C. Gay, Europhys. Lett, **15**, 697 (1991) 2.1

[26] J. C. Gay, D. Delande and A. Bommier, Phys. Rev. A, **39**, 6587 (1989) 2.1

[27] W. Pauli, Z. Phys.36, 339 (1926), English translation in B. L. van der Waerden (Editor) Sources of quantum mechanics (Courier Dover Publications: New York) (1968) 2.2.1, 2.2.1, 3.1

[28] M. J. Engelfield, Group Theory and the Coulomb Problem, Wiley, New York (1972) 2.2.1

[29] Y. N. Demkov, B. S. Monozon and V. N. Ostrovsky, Sov. Phys. JETP, **30**, 775 (1969) 2.2.1, 2.2.1

[30] Y. N. Demkov, V. N. Ostrovsky and E. A. Solov'ev, Sov. Phys. JETP **39**, 57 (1974) 2.2.1, 2.2.1

[31] A. K. Kazansky and V. N. Ostrovsky, J. Phys. B **29**, L855 (1996) 2.2.1, 2.2.1, 2.2.1, 2.2.2, 5

[32] E. Majorana, Nuovo Cimento 9, 43 (1932) 2.2.1

[33] L. D. Landau and E. M. Lifschits, Quantum Mechanics, Pergamon Press (1976) 2.2.1

[34] M. Førre, H. M. Nilsen, and J. P. Hansen, Phys. Rev. A, **65**, 053409 (2002) 2.2.1, 2.2.2, 3.5, 3.11, 5

[35] H. A. Bethe and E. E. Salpeter, Quantum Mechanics of One- and Two-Electron Atoms, Springer Verlag (1957) 2.3.2, 3.5

[36] T. A. Delchar, Vacuum Physics and Techniques, 1985-95. (Chapman and Hall, 1993) 3.1.1

[37] Kurt J. Lesker and Company. Turbomolecular Pumps and Drag Pumps: Technical Notes. http://www.lesker.com. (2004) 3.2

[38] PFEIFFER VACUUM, Translation of the Orignal operating Instructions, Compact Turbo^{TM} technical Manual, http://www.ptb-sales.com/manuals/balzers/tmu261p.pdf 3.1.1

[39] Leybold Turbovac Operating Instructions. TURBOVAC 50 technical Manual *www.idealvac.com/files/Leybold_Turbovac_Operating_Instructions.pdf* 3.1.1, B

[40] Leybold Turbotronik NT10, Electronic Frequency Converter Operating Instructions Manual B

[41] W. L. Fuqua and K.B.MacAdam, Rev. Sci. Instrum, **56**, 385 (1985) 3.3.3

[42] M. Førre and J. P. Hansen, Phys. Rev. A, **67**, 053402 (2003) 3.4, 3.4, 3.5, 3.20

[43] E. Horsdal, Rydberg atoms Production and multiphoton processes 3.8

[44] M. Førre, Rydberg Atoms in External Time Dependent Fields, MSc thesis, University of Bergen, (2000) 3.5

[45] F. Robicheaux, C. Wesdrop and L. D. Noordam, Phys. Rev. A, **62**, 043404 (2000) 3.4

[46] W. E. Cooke and T. F. Gallagher, Phys. Rev. A, **17**, 1226 (1978) 3.5

[47] *http://www.photonis.com/upload/industryscience/pdf/electron_multipliers/ChannelBook.pdf* 3.12

[48] G. W. Goodrich, W. C. Wiley, Rev. Sci. Instrum, **33**, 761 (1962) 3.6

[49] M. G. Littman and H. J. Metcalf, Appl. Opt. **17**, 2224 (1978) 3.7.1, 3.7.1

[50] S. B. Hansen, Electron Capture from Oriented Circular Rydberg Atoms, PhD thesis, University of Aarhus, (1993) 3.7.1

[51] M. Qhobosheane, Introduction to Spectroscopy in the Teaching Lab Using Ocean Optics Spectrometers, Ocean Optics. Inc (2006) 3.7.2

[52] D. S. King, P. K. Schenck, K. C. Smyth and J. C. Travis, Appl. Opt, **16**, 2617 (1977) 3.7.3

[53] K. S. Mogensen, Theoretical and Experimental Investigations of the Production of Elliptic States of Lithium Rydberg Atoms with Special Emphasis on the Effects of Quantum Defects, master thesis, (1994) 3.11

[54] T. F. Gallagher and W. E. Cooke. Phys. Rev. Lett, B, **42**, 835 (1979) 3.8

[55] W. E. Cooke and T. F. Gallagher, Phys. Rev. A, **21**, 588 (1980) 3.8

[56] P. R. Koch, H. Hieronymus, A. F. J. Van Raan, W. Raith, Physics Letters A, **75** 273 (1980) 3.8

[57] X. Lu, Y. Sun and H. Metcalf Phys. Rev. A, **84**, 033402 (2011) 3.8

[58] R. F. Stebbings, F. B. Dunning and T. F. Gallagher, Rydberg States of Atoms and Molecules, University Press, Cambridge (1983) 3.8

[59] *http://physics.nist.gov/PhysRefData/ASD/lines_form.html* 3.9

[60] H. Ishii, K. Sugiyama, E. Ito, and K. Seki, Adv. Mater, **11**, 605 (1999)

[61] T. Yabuzaki, Y. Nakayama, Y. Murakami and T. Ogawa, Phys. Rev. A, **10**, 1955 (1974) 3.14

[62] T. Yabuzaki, Y. Murakami and T. Ogawa, J. Phys. B, **9**, 9 (1976) 6

[63] L. Sælen, Quantum control of strongly coupled dynamics in few component systems, PhD thesis (2009) 6
C